Precessional magnetization dynamics in micron sized ferromagnetic elements

Rietjens, J.H.H.

Award date:
2004

Def. Verlag

TU/e technische universiteit eindhoven

Eindhoven University of Technology
Department of Applied Physics
Group Physics of Nanostructures

Title: **Precessional magnetization dynamics in micron sized ferromagnetic elements**

Author: *J.H.H. Rietjens*

Date: April 2004

Report of a graduation project, carried out in the Group Physics of Nanostructures of the Department of Applied Physics at the Eindhoven University of Technology, from March 2003 till April 2004.

FNA

Supervisor: C. Józsa b.sc
Professor: prof. dr. B. Koopmans

Abstract

In the last decades, the demand for digital storage capacity and high-speed memories has increased exponentially. Many of these devices use the orientation of the magnetization of small magnetic elements to store binary data and, as the switching times and dimensions of these elements decrease, it is crucial to understand the fast magnetization dynamics.

In this work, a measurement scheme based on the pump-probe technique has been developed, which allows for time-resolved imaging of the magnetization vector in microscopic magnetic elements with a spatial resolution of 1 μm. The components of the magnetization vector were detected separately and simultaneously, via the magneto optical Kerr effect. Precessional magnetization dynamics is induced in ferromagnetic elements by short (<1ns) magnetic field pulses. These magnetic field pulses are generated by applying voltage pulses to the strip lines, on top of which the magnetic elements were deposited by means of optical lithography.

The validity of the vectorial measurement technique was first verified by small angle precessional dynamics measurements on relatively large Permalloy dots. The observed dynamics resulting from magnetic field pulses agrees well with the expectation from a numerical model, based on the Landau-Lifshitz-Gilbert-equation. The actual magnetic pulse shape was calculated from the measurement data and turned out to be similar to the shape of the voltage pulses.

The same measurement technique was used to study magnetization dynamics in real magnetic tunnel junction (MTJ) elements. The spatial resolution of ~1 μm allowed for imaging the magnetization dynamics of the whole element. An interesting spatially inhomogeneous dynamics is observed in the element, which we attribute to a competition between the different local magnetic fields acting on the spins.

Other phenomena, such as enhanced damping of the precessional motion at the edges of the element, the apparent existence of a second spin mode that shows up at high external bias fields, and an increased decoherence of spin motion across the laser spot will be shown. Possible mechanisms for these phenomena and suggestions for further research will be given. Large angle excitations of the magnetization in these elements will be demonstrated, and possible ways to perform switching experiments in these elements will be discussed.

Contents

Abstract ..... **i**

Contents ..... **iii**

1 Introduction **1**

2 Theory **5**

2.1 Precessional dynamics of a macrospin 5

2.2 Modeling the influence of a magnetic field pulse 9

2.3 Calculating the shape of the magnetic field pulse 12

2.4 Large angle excitations and precessional switching 13

2.5 Coupling effects in micromagnetic structures 16

3 Experimental Setup **19**

3.1 Magnetic samples 19

3.1.1 Circular Py dots on a coplanar waveguide 21

3.1.2 Rectangular magnetic tunnel junctions on a current line 22

3.2 Optical techniques 26

3.2.1 Magneto-Optical Kerr Effect 26

3.2.2 Static MOKE 28

3.2.3 Time-resolved MOKE 30

3.2.4 Vectorial TRMOKE 33

4 Results **37**

4.1 Demonstration of the vectorial TR-MOKE setup 37

4.2 Calculation of the field pulse profile 42

4.3 Bias field dependence of the precessional motion 45

4.4 Large angle excitations 50

4.5 Spatially resolved measurements 54

5 Conclusions and outlook **61**

Acknowledgements **63**

Bibliography **65**

1 Introduction

Since the era of magnetic data storage has begun, the ability to manipulate the magnetization of small magnetic elements is under constant investigation. In magnetic storage devices, the orientation of the magnetization of a magnetic element is used to store binary data. For example, a magnetic element with a magnetization vector parallel to a certain axis can represent a "0" and an element with an anti-parallel magnetization a "1". These storage devices include floppy disks, hard-disk drives and also magnetic random access memory (MRAM), which is currently being developed. The constant need for faster recording devices with higher capacity resulted in large research efforts to scale down the size of the magnetic elements and to decrease the switching time of the magnetization of these elements.

The bit-length in commercially available hard-disk drives, for example, decreased from ~250 μm to below 0.04 μm in the past 40 years. The information density increased from 2 kbit/inch^2 to 170 Gbit/inch^2. A major breakthrough in this advance has been the discovery of the Giant MagnetoResistance (GMR) effect [1]. It was discovered that two thin ferromagnetic (FM) layers, separated by a non-magnetic (NM) metal layer, have a lower resistance when their magnetizations are oriented parallel than when they are oriented anti-parallel, see Figure 1.1. Nowadays, FM-NM-FM trilayers can be grown that exhibit a GMR effect at room temperature of 17% [2]. When used as a magnetic sensor in hard-disk heads, the GMR effect allows for much smaller element sizes and much faster readout than was previously possible.

In MRAM, another resistance effect is used, namely the Tunnel MagnetoResistance (TMR) effect. In this case, the tunnel current of electrons between two magnetic layers, separated by a very thin (1 – 2 nm) insulating barrier, is strongly dependent on the orientation of the magnetization of the two layers [3]. When the FM-layers are made of the same material, a parallel alignment has a lower resistance than the anti-parallel alignment. At room temperature, this effect can be as high as 70% when transition metals are used as magnetic layers [4].

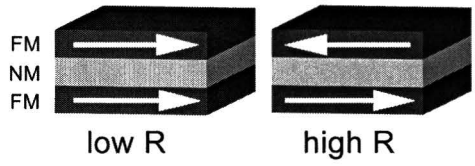

Figure 1.1: The resistance of FerroMagnetic / Non-Magnetic / FerroMagnetic trilayers depends on the orientation of the magnetization in the ferromagnetic layers. A parallel orientation has a lower resistance than an anti-parallel one.

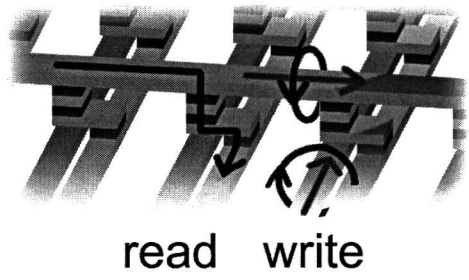

Figure 1.2: Impression of a MRAM architecture, in which the resistance of a MTJ between two perpendicular lines is measured to read the magnetic state of the MTJ. The magnetic state of the MTJ can be written by sending current through the two perpendicular lines to produce a total field that is enough to switch only one of the FM-layers. Adapted from [5].

The two magnetic layers and the tunnel barrier form a magnetic tunnel junction (MTJ) that can be used as a storage cell of one bit. A matrix of these MTJ's can then form a magnetic memory. Write operations are carried out with a magnetic field produced by two crossed current lines to address each element of the matrix. CMOS technology is used to read out the resistance and thus the magnetic state of each element, as well as to switch between read and write cycles [6]. A schematic layout of the MRAM currently in development is shown in Figure 1.2. The magnetic state of a MTJ is stationary in time and does not need any current, so the MRAM is a non-volatile memory. This non-volatility in combination with large memory capacity, fast switching and random accessibility makes MRAM a very promising memory concept for the near future. Since the size of the MTJ-elements can be easily decreased below one micron, very dense arrays of MTJ's can already be made to form a MRAM. Motorola recently announced the production of a 4 Mbit MRAM, with switching times of 15 ns (66 MHz) [7]. This is, however, not fast and not dense enough to compete with existing volatile memories, such as DDR SDRAM or RDRAM that operate at 800 MHz with capacities of 1 Gb. Therefore, ways for faster switching are being explored.

In conclusion, there is a strong need for reduced magnetic element sizes and very fast switching. This, however, introduces complications. With micron-sized elements, edge effects already become important and these effects can influence the magnetic behavior of the whole element. As an example, magnetization reversal may become non-uniform over the element, which can lead to longer switching times or even unstable switching. The shape of such small elements is an important property that can be used to minimize the non-uniformities and to assure stable switching.

On the other hand, as the switching times approach the sub-nanosecond regime, the magnetization reversal mechanism also changes. Slow (sub-)microsecond switching is dominated by domain wall movement and the resulting growth and shrinking of different

domains. At shorter switching times, the reversal becomes a relaxation dominated precession-like behavior. MRAMs currently being developed operate in this regime, because the current pulses, used to generate the magnetic field that switches the element, are relatively long. Finally, in the sub-nanosecond regime, the motion of the magnetization vector is precession dominated and the fundamental limit of the switching time is half the period of the precession. This means, again for the MRAM case, that in order to achieve such fast switching, very short (< 1 ns) current pulses have to be applied. Consequently, it is of critical importance to know the exact behavior of the magnetization vector during a switching event in these small magnetic elements. Furthermore, precise knowledge of the magnetic field pulse that is produced with current lines is also needed, since the motion of the magnetization vector depends strongly on the pulse shape and duration.

This Thesis is concerned with the issues mentioned above. Chapter 2 will describe the theory of precessional magnetization dynamics and show some simulations to explain the influence of the magnetic field pulse, external bias field, damping parameter and sample properties on the magnetization dynamics. Edge effects and spin modes that describe spatial non-uniformities of the dynamics will be discussed as well.

The experimental techniques that have been used in this work will be presented in Chapter 3. The electrical-pump / optical-probe scheme used to achieve a temporal resolution below 10 ps and spatial resolution of 1 μm in combination with a vectorial measurement scheme will be explained. The samples on which the experiments have been performed, consisting of micron-sized magnetic elements deposited on current lines, will also be discussed in detail in this chapter.

Chapter 4 will present the experimental results obtained with the magnetic samples. The accuracy of the vectorial measurement scheme will be demonstrated and the magnetization dynamics resulting from different magnetic field pulses will be discussed. Spatial non-uniformities in the small magnetic elements and their effect on the dynamics will be addressed as well. Furthermore, it will be demonstrated that measurements of the magnetization dynamics can give information about the static state of the magnetization in magnetic elements.

Finally, Chapter 5 will summarize the main conclusions that can be drawn from this work and give recommendations for future research.

2 Theory

As may have become clear from the introduction, detailed knowledge about the process of magnetization reversal, especially in the precession dominated regime, is crucial in order to achieve switching of the magnetization below one nanosecond. Size and shape effects also play an important role in the reversal process of the magnetic element in question. This chapter will address both issues and the relevant physics will be explained.

First, the equation of motion for the magnetization vector in the precession dominated regime is introduced. The relevant parameters in this equation will be discussed and some simulations from a numerical model will be shown. A set of formulas will be deduced that can be used to extract the magnetic pulse shape from the measured response of the magnetization. The numerical model will also be used to show how magnetization reversal with magnetic field pulses can be achieved. This chapter will conclude with a discussion of the magnetic interactions that give rise to non-uniform behavior of spins in micron-sized magnetic elements, which become more and more important when the size of the magnetic elements decreases. Interlayer coupling, present in magnetic devices, will be addressed and shape effects in the form of demagnetizing fields will be discussed. The concept of spin-modes is introduced, with respect to the case of the so-called edge modes.

2.1 Precessional dynamics of a macrospin

The magnetization dynamics on a (sub-)nanosecond timescale is governed by the Landau-Lifshitz-Gilbert equation [8]. This equation describes the motion of a single magnetization vector. In order for this equation to describe accurately the dynamics in a microscopic magnetic element, the element in question must act as a *macrospin*. In other words, the magnetic element must be a single-domain particle to a large extend. All the spins in the element will then behave coherently, which allows treating them as a single magnetization vector. In practice, this condition can be met by applying a strong external

magnetic field that aligns all the spins of a magnetic element along the direction of this external field.

Before introducing the full equation, we will first take a look at the Landau-Lifshitz form of the equation, which contains no damping term. Starting with elementary quantum mechanics it can be deduced [9] that the equation of motion of a macrospin is

$$\frac{d\vec{M}(t)}{dt} = \gamma\mu_0\left[\vec{M}(t)\times\vec{H}(t)\right], \tag{2.1}$$

where $\vec{M}(t)$ is the magnetization vector of the macrospin, γ the gyromagnetic ratio ($\gamma = ge/2m_e$, with g the gyromagnetic splitting factor of the electron in the magnetic material, and e and m_e the electron charge and mass respectively), μ_0 the magnetic permeability of vacuum and $\vec{H}(t)$ the effective magnetic field acting upon the macrospin. This equation states that the effective magnetic field exerts a torque on the magnetization and this torque is responsible for the motion of the magnetization. Assuming that the effective field is time-independent, $\vec{H}(t) = \vec{H}$, multiplying (2.1) with $\vec{M}$ and $\vec{H}$ resp. leads to

$$\frac{d}{dt}\left[\vec{M}(t)\right]^2 = 0; \frac{d}{dt}\left[\vec{M}(t)\cdot\vec{H}\right] = 0, \tag{2.2}$$

which shows that the length of the magnetization vector does not change and that the angle between the directions of the magnetization and the effective field remains constant. Equations (2.1) and (2.2) resp. thus describe a precessional motion around the direction of the effective field $\vec{H}$.

The frequency of this precession can be calculated as follows. We consider the case of a magnetic element with dimensions small enough to exhibit shape anisotropy in all three directions. Separating the components of (2.1) for the case with the x-direction aligned along the direction of a static field H_x^0, gives to first order (small perturbation, so M_x = constant = M_s, with M_s the saturation magnetization of the magnetic element)

$$\begin{aligned} \dot{M}_x &= 0 \\ \dot{M}_y &= \gamma_0(M_x H_z - M_z H_x) \\ \dot{M}_z &= -\gamma_0(M_x H_y - M_y H_x) \end{aligned}, \tag{2.3}$$

where a dot represents differentiation with respect to time. Also, the quantity γ_0 is introduced, which is defined as

$$\gamma_0 = \mu_0 \frac{g|e|}{2m} = -\mu_0\gamma. \tag{2.4}$$

The static field H_x^0 can include an applied bias field, exchange- and interlayer coupling fields. The components of the effective field $\vec{H}$ are

$$H_x = H_x^0 - N_x M_x;\;\; H_y = -N_y M_y;\;\; H_z = -N_z M_z, \tag{2.5}$$

with N_i the demagnetization factors in the direction i, which arise due to the shape anisotropy. With (2.5), the last two lines of equation (2.3) become

$$\begin{aligned} \dot{M}_y &= -\gamma_0 \left[(N_z - N_x) M_s + H_x^0 \right] M_z \\ \dot{M}_z &= \gamma_0 \left[(N_y - N_x) M_s + H_x^0 \right] M_y \end{aligned} . \tag{2.6}$$

This set of coupled differential equations has solutions that describe harmonic oscillations (time-dependence $\exp(-i\omega t)$), if the determinant of the coefficients vanishes. This leads to

$$\omega = -\gamma_0 \sqrt{\left[(N_z - N_x) M_s + H_x^0 \right] \left[(N_y - N_x) M_s + H_x^0 \right]}, \tag{2.7}$$

the Kittel-formula for the frequency of the precession [10]. The precession frequency thus depends on the static field H_x^0 and on the properties of the magnetic element, such as shape and saturation magnetization. It must be noted that in this analysis, other properties of the magnetic element, such as crystalline anisotropies, are not taken into account.

In real physical systems this precessional motion will not last forever. Therefore, equation (2.1) has to include a damping term, such that the magnetization will align with the static field in a finite time. The usual way to do this is to include a dissipation term in the effective field $\vec{H}(t)$,

$$\vec{H}(t) \rightarrow \vec{H}(t) + \alpha \frac{1}{\gamma_0 M_s} \frac{d\vec{M}(t)}{dt}, \tag{2.8}$$

with α a phenomenological parameter, called the Gilbert damping parameter. Depending on the value of α, the precessional motion can be over-damped, critically damped or under-damped. In most cases with thin magnetic layers, $\alpha \ll 1$, and the motion is in the under-damped regime. Inserting (2.8) in (2.1) leads to

$$\frac{d\vec{M}(t)}{dt} = -\gamma_0 \left[\vec{M}(t) \times \vec{H}(t) \right] + \frac{\alpha}{M_s} \left[\vec{M}(t) \times \frac{d\vec{M}(t)}{dt} \right]. \tag{2.9}$$

This is the Landau-Lifshitz-Gilbert (LLG) equation that fully describes the motion of a macrospin. In general, it is impossible to solve this equation analytically. However, when we consider only small perturbations, for instance long after a magnetic disturbance, the solutions to this equation are damped harmonic oscillations,

$\exp(i\omega t - t/\tau)$. Here, τ is the characteristic time of the exponential decay. To prove this fact, we separate equation (2.9) in the three spatial components, with again the assumption $M_x = M_s = constant$:

$$\begin{aligned} \dot{M}_x &= 0 \\ \dot{M}_y &= \gamma_0(M_x H_z - M_z H_x) - \alpha \dot{M}_z \\ \dot{M}_z &= -\gamma_0(M_x H_y - M_y H_x) + \alpha \dot{M}_y \end{aligned} \quad . \tag{2.10}$$

When we consider a thin film with a strong in-plane anisotropy ($N_x = N_y = 0$, $N_z = 1$), the demagnetizing field is given by $H_{dem} = -N_z M_z = -M_z$. With a static field H_x^0 in the x-direction, equation (2.10) becomes

$$\begin{aligned} \dot{M}_x &= 0 \\ \dot{M}_y &= \gamma_0(M_s + H_x^0) M_z - \alpha \dot{M}_z \\ \dot{M}_z &= -\gamma_0 H_x^0 M_y + \alpha \dot{M}_y \end{aligned} \quad . \tag{2.11}$$

As trial solutions we take $M_y = \cos(\omega t)\exp(-t/\tau)$ and $M_z = \varepsilon \sin(\omega t + \varphi)\exp(-t/\tau)$. These solutions represent a damped precessional motion. The ellipticity ε is included to account for a strong elliptical precession. The phase factor φ is essential, as it can be shown that a trial solution with $\varphi = 0$ is not a solution of (2.11). Inserting these trial solutions into (2.11) and demanding that the prefactors of the $\cos(\omega t)$ - and $\sin(\omega t)$ -terms are equal, yields a set of four equations for the unknown parameters ω, τ, ε and φ:

$$\begin{aligned} -\frac{1}{\tau} &= -\varepsilon\gamma_0\left(M_s + H_x^0\right)\sin\varphi - \omega\varepsilon\alpha\cos\varphi + \frac{\varepsilon}{\tau}\alpha\sin\varphi \\ -\omega &= -\varepsilon\gamma_0\left(M_s + H_x^0\right)\cos\varphi + \omega\varepsilon\alpha\sin\varphi + \frac{\varepsilon}{\tau}\alpha\cos\varphi \\ \omega\varepsilon\cos\varphi - \frac{\varepsilon}{\tau}\sin\varphi &= \gamma_0 H_x^0 - \frac{\alpha}{\tau} \\ -\omega\varepsilon\sin\varphi - \frac{\varepsilon}{\tau}\cos\varphi &= -\omega\alpha \end{aligned} \quad . \tag{2.12}$$

This set of equations can be solved with the result

$$\begin{aligned} \omega &= \gamma_0 \frac{\sqrt{4H_x^0(H_x^0 + M_s) - \alpha^2 M_s}}{2(1+\alpha^2)}, \tau = \frac{2(1+\alpha^2)}{\gamma_0\alpha(2H_x^0 + M_s)} \\ \varphi &= arc\sec\left(\frac{2\sqrt{H_x^0(H_x^0 + M_s)}}{\sqrt{4H_x^0(H_x^0 + M_s) - \alpha^2 M_s}}\right), \varepsilon = \sqrt{\frac{H_x^0}{H_x^0 + M_s}} \end{aligned} \quad . \tag{2.13}$$

This proves that the trial functions are indeed solutions of (2.11). In the limit $\alpha^2 \ll 1$, (2.13) simplifies to

$$\omega = \gamma_0 \sqrt{H_x^0 (H_x^0 + M_s)}, \tau = \frac{2}{\gamma_0 \alpha (2H_x^0 + M_s)}$$
$$\varphi = \frac{\alpha M_s}{\sqrt{4H_x^0 (H_x^0 + M_s)}}, \varepsilon = \sqrt{\frac{H_x^0}{H_x^0 + M_s}} \quad . \tag{2.14}$$

Let us consider two different limits, when $H_x^0 \ll M_s$ and when $H_x^0 \gg M_s$. In the first case, $H_x^0 + M_s \simeq M_s$ and we see that the decay time is independent of the frequency and that the frequency increases with the square root of the static field, H_x^0. ε is much smaller than unity, indicating a strong elliptical motion due to the demagnetization field, and the phase factor φ is proportional to α, thus also small. In the latter case, $H_x^0 + M_s \simeq H_x^0$ and we see that $\omega \simeq \gamma_0 H_x^0$ and $\tau \simeq 1/\alpha\omega$. The frequency thus increases linear with the static field and the decay time is inversely proportional to the frequency. This implies that the number of oscillations of the magnetization in the characteristic time is constant. The ellipticity approaches unity, indicating a circular precessional motion. In this work, the situation will always be close to the first limit, when $H_x^0 \ll M_s$.

2.2 Modeling the influence of a magnetic field pulse

In storage devices, short magnetic field pulses have to be induced in magnetic elements in order to switch the magnetization of these elements in the sub-nanosecond regime, as mentioned in the introduction. The motion of the magnetization under the action of these field pulses can, of course, not be described by exponentially damped oscillations. In order to gain insight into the full response of a macrospin, also during the time a field pulse of arbitrary shape is present, a numerical model is developed that integrates the LLG-equation. For this purpose, another form of the LLG-equation is more practical. Equation (2.9) can be rewritten as

$$\left(1+\alpha^2\right)\frac{d\vec{M}(t)}{dt} = \gamma_0 \left[\vec{M}(t) \times \vec{H}(t)\right] + \frac{\alpha\gamma_0}{M_s}\left[\vec{M}(t) \times \left[\vec{M}(t) \times \vec{H}(t)\right]\right]. \tag{2.15}$$

With this form of the LLG-equation, the motion of the macrospin $\vec{M}(t)$ can be calculated if the time-dependent field $\vec{H}(t)$ and the material parameters α, M_s and γ_0 are known. It is particularly useful for application in numerical models, as it can be linearized in order to obtain a relationship between the magnetization and magnetic field on $t = t_i$ and the magnetization on $t = t_i + \Delta t$, with Δt the time step in the numerical model.

Our model calculates the magnetization dynamics in a thin Permalloy ($Ni_{81}Fe_{19}$) film under the action of a magnetic field pulse. The length of the magnetization vector is

kept constant. The magnetic fields acting on the macrospin that are included in the model, are shown in Figure 2.1. The static field only consists of an external bias field, H_{bias}, applied along the x-axis and consequently this defines the initial direction of the magnetization $\vec{M}$. The magnetic field pulse H_{pulse} is applied along the y-axis, perpendicular to the initial magnetization and thus creating a maximum torque. As anisotropy fields we consider only the strong in-plane anisotropy ($N_x = N_y = 0$, $N_z = 1$), which yields a demagnetization field only in the z-direction, $H_{dem} = -N_z M_z = -M_z$. The effective field $\vec{H}$ that acts on the macrospin is thus

$$\vec{H}(t) = \left(H_x, H_y, H_z\right) = \left(H_{bias}, H_{pulse}(t), -M_z(t)\right) \tag{2.16}$$

The values for the material parameters α and M_s that correspond to Permalloy are obtained from literature: $\alpha = 0.01$ and $M_s = 900$ kA/m [11].

In Figure 2.2 are plotted the responses of the magnetization to different magnetic field pulses and with a bias field of 2.4 kA/m. This bias field yields a precession frequency of 1.7 GHz according to (2.14), thus a precession period of 0.6 ns. As field pulse examples are taken a "step-edge", a rectangular pulse of 1.5 ns (longer than the precession period) and a rectangular pulse of 0.25 ns (shorter than the precession period). In each case, the magnetic field pulse starts at $t = 0$ and $\left|H_{pulse}\right|_{\max} = 0.44$ kA/m. Due to the field pulse, the y-component of the effective field changes from zero to H_{pulse} and the new effective field $\vec{H}_{new}$ makes an angle $\varphi = \arctan\left(\left|H_{pulse}/H_{bias}\right|\right)$ with the x-axis. This triggers a precessional motion around $\vec{H}_{new}$.

In the "step-edge" case, the magnetization equilibrates after some time in the direction of $\vec{H}_{new}$. In the 1.5 ns pulse case, the magnetization first starts a precession around $\vec{H}_{new}$, but after the pulse ends the direction of the effective field is again the x-direction. Consequently, the magnetization starts to precess around the x-axis, which is the final equilibrium direction. In the 0.25 ns case, the pulse duration is too short for the magnetization to complete a full oscillation around $\vec{H}_{new}$ and after an initial excitation the magnetization precesses around the x-axis and finally damp out.

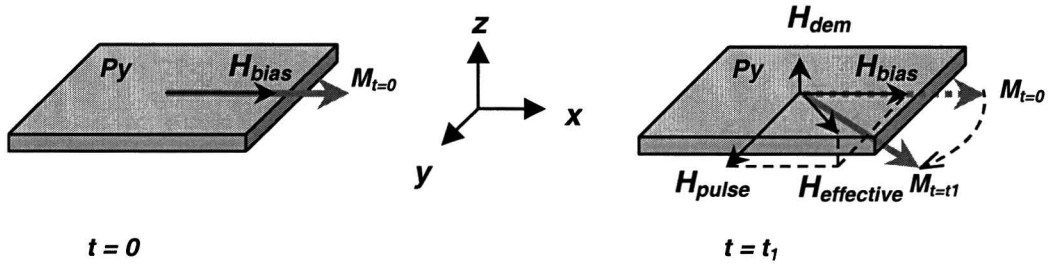

Figure 2.1: Geometry used in the numerical LLG-model to simulate magnetization dynamics. External bias field and initial magnetization of the Py-element are in the x-direction, the field pulse is applied in the y-direction. The resulting effective field, demagnetization field and motion of the magnetization are also indicated.

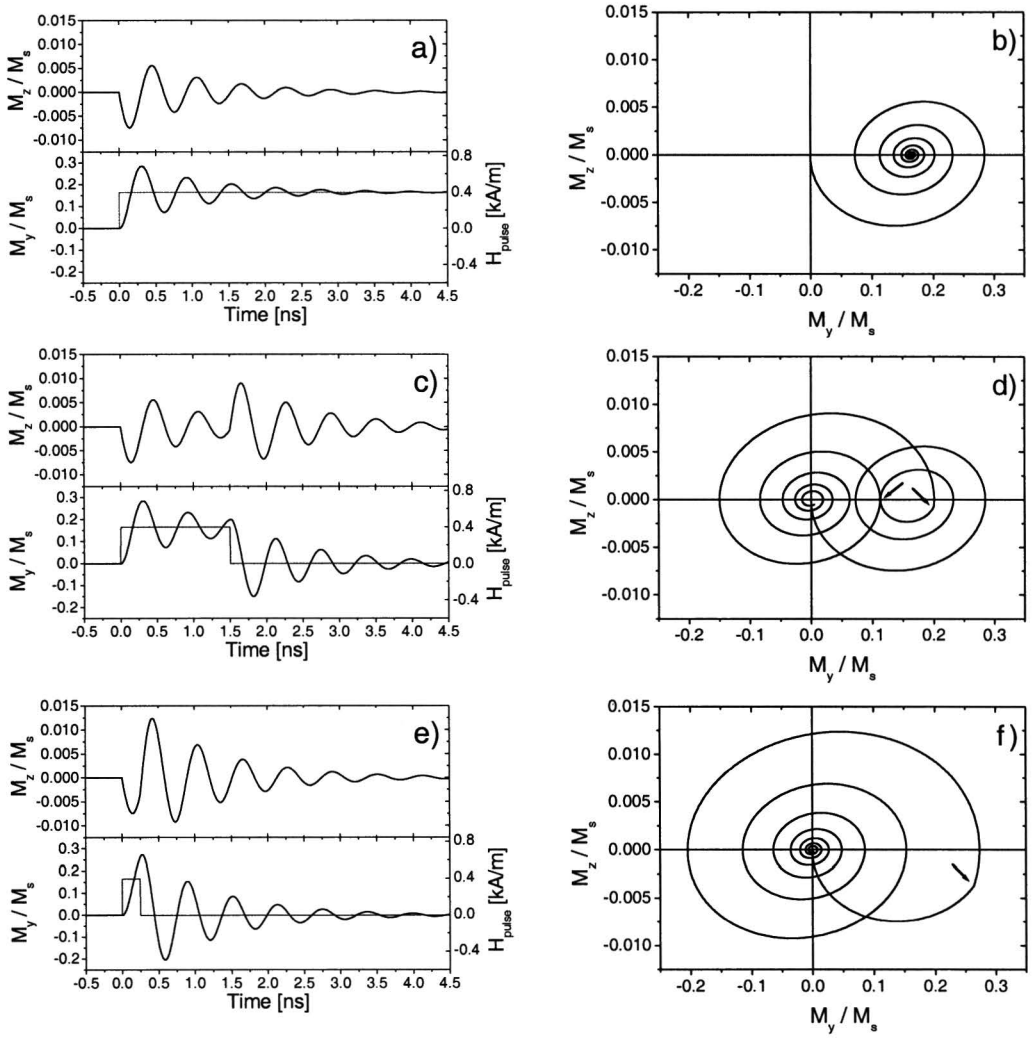

Figure 2.2: The responses of the magnetization due to different magnetic field pulses are plotted in a m_y-t-, m_z-t- and m_z-m_y-graph. The figures show the response to a step pulse, (a) and (b), a 1.5 ns pulse, (c) and (d), and a 0.25 ns pulse (e) and (f). In (a), (c) and (e) also the field pulse is plotted. The right arrows in (d) and (f) indicate the end of the field pulse.

The M_z-M_y-plots show even more clearly this precessional motion around $\vec{H}_{new}$ and around the x-axis. Especially in the 1.5 ns case, the amplitude of the final precession around the x-axis depends heavily on the pulse duration. From Figure 2.2d it can be seen that the moment the pulse ends (right arrow), the magnetization reaches its maximum deviation from the x-axis. This results in a large torque as the effective field returns to the x-axis, and in a precession with large amplitude. If the pulse had ended somewhat earlier (left arrow) the angle between the magnetization and the x-axis would have been smaller, resulting in a smaller torque and a precession of lower amplitude around the x-axis. Note also that the M_z scale is an order of magnitude smaller than the M_y scale, so that the precession is in fact strongly elliptical, as expected from (2.14). In each case, long after the last pulse edge, damped oscillations can be seen, in agreement with our previous analysis.

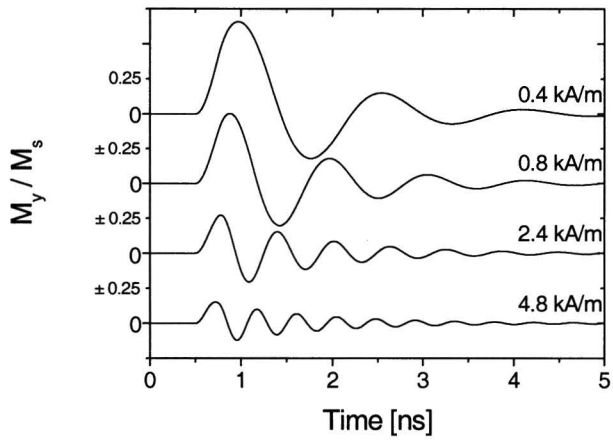

Figure 2.3: Bias field dependence of the precessional motion of the magnetization. The frequency and amplitude of the oscillation of the M_y-component increase and decrease resp. as the bias field increases.

Besides the pulse shape, the effect of different bias fields is also investigated with the model. Figure 2.3 shows the magnetization response to a field pulse of 0.25 ns with different bias field strengths. Two features can be seen from these graphs. First, the amplitude of the oscillation drops as the static field increases. At higher static field, the change of the effective field due to the magnetic field pulse, $\varphi = \arctan\left(\left|H_{pulse}/H_{bias}\right|\right)$, is rather small. The magnetization vector rotates around $\vec{H}_{new}$ and can thus make a maximum angle with the x-axis of 2φ (when $\alpha = 0$), thus the precession amplitude in M_y is $M_{y,\max} = \sin(2\varphi)$. The amplitude has a maximum if $\varphi = 45°$ (H_{pulse} / H_{bias} = 1) and drops to 0 when H_{pulse} / $H_{bias} \rightarrow 0$ and H_{pulse} / $H_{bias} \rightarrow \infty$. Second, the frequency of the oscillations increases as the static field increases. The frequency of the precession is given by (2.14), with $H_x^0 = H_{bias}$ and increases with the square root of the bias field, since $H_{bias} \ll M_s$.

2.3 Calculating the shape of the magnetic field pulse

Usually, as is the case with experiments, the response of the magnetization to a certain magnetic field pulse is measured, whereas the exact form of this magnetic field pulse is unknown. As mentioned in the introduction, if one really wants to control the magnetization, knowledge of the precise form of magnetic field pulse is of crucial importance. In this case, the form (2.9) of the LLG equation can be used to solve this problem [12].

The unknown parameter in the equation is the magnetic field pulse profile, and the (measured) magnetization data is used as input to extract this pulse profile. Under the assumption of a small perturbation from equilibrium, which is e.g. the case with a high static field, we can separate equation (2.9) into the three spatial directions, as in equation (2.10). When we consider only the static field H_{bias}, the field pulse H_{pulse} and the

demagnetization field H_{dem} as we did in the numerical model, the last two lines of equation (2.10) become

$$\begin{aligned} \dot{M}_y &= \gamma_0 (M_s + H_{bias}) M_z - \alpha \dot{M}_z \\ \dot{M}_z &= \gamma_0 (M_s H_{pulse}(t) - M_y H_{bias}) + \alpha \dot{M}_y \end{aligned} . \tag{2.17}$$

These equations can be solved for $H_{pulse}(t)$, with the resulting formulae containing either M_y or M_z (and their integrals or derivatives):

$$H_{pulse}(t) = -\frac{\alpha^2 + 1}{\gamma_0^2 (M_s + H_{bias})} \ddot{m}_y - \frac{\alpha (M_s + 2H_{bias})}{\gamma_0 (M_s + H_{bias})} \dot{m}_y + H_{bias} m_y , \tag{2.18}$$

$$H_{pulse}(t) = \frac{\alpha^2 + 1}{\gamma_0} \dot{m}_z + \alpha (M_s + 2H_{bias}) m_z + \gamma_0 H_{bias} (M_s + H_{bias}) \int_{-\infty}^{t} m_z dt , \tag{2.19}$$

where $m_i = M_i / M_s$. Of course, if data of M_y and M_z are both available, $H_{pulse}(t)$ can be easily extracted from the last line of equation (2.17) and it follows that

$$H_{pulse}(t) = \frac{1}{\gamma_0} \left(\dot{m}_z - \alpha \dot{m}_y \right) + H_{bias} m_y . \tag{2.20}$$

The above formulae will be used in this work to extract the pulse profile from measurement data on small angle precessional motion, where the assumption $M_x = M_s = constant$ holds.

2.4 Large angle excitations and precessional switching

Until now, only small angle excitations of a macrospin have been considered. These small angle excitations occur whenever the static magnetic field is much larger than the applied magnetic field pulse. However, when the field pulse becomes comparable to or larger than the static field, large angle excitations may occur. The magnetization then rotates significantly in the plane of the elements. Large angle excitations can also be simulated with the numerical model. When the ratio between the bias field and the field pulse is reduced to 0.5 (H_{bias} = 0.4 kA/m, H_{pulse} = 0.8 kA/m) and the 0.25 ns magnetic pulse shape is used, the result is an excitation of the magnetization up to 85°, as shown in Figure 2.4. Due to the bias field, the initial and final directions of the magnetization are the same.

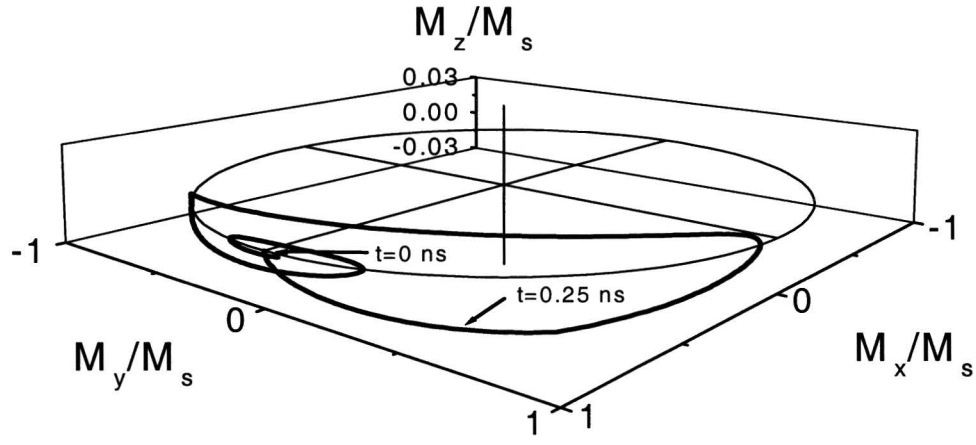

Figure 2.4: Simulated large angle excitation (85°) of the magnetization with a field pulse of 0.25 ns duration and an amplitude of 0.8 kA/m. The bias field is in the x-direction and equal to 0.4 kA/m.

The most interesting large angle excitation is the one that results in a switch of the magnetization (180° rotation). A stable switch can only occur when the magnetic element has two stable states of opposite magnetization direction. This implies that the external bias field must be absent and that the magnetic element must have a uniaxial anisotropy. In this case, the geometry is slightly different than discussed before, as visualized in Figure 2.5.

The initial magnetization is aligned along the x-axis due to a uniaxial in-plane anisotropy and the field pulse is applied along the y-axis. The torque due to the field pulse lifts the magnetization out of the plane, which introduces a large demagnetization field. The demagnetization field then becomes the dominant component of the effective field after the field pulse ends. The torque now has a strong component in the y-direction and as a result the magnetization rotates in the plane.

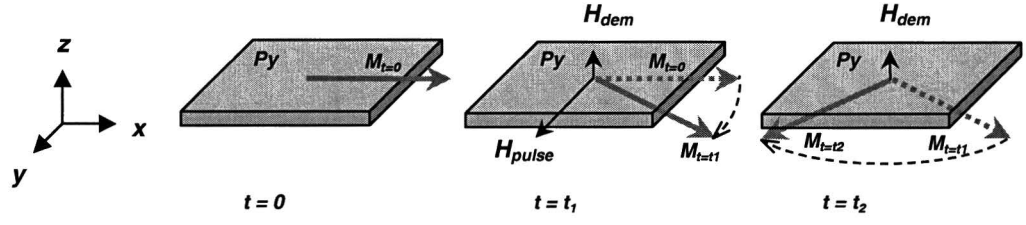

Figure 2.5: Geometry used in the numerical LLG-model to simulate switching of the magnetization. The initial magnetization of the Py-element is in the x-direction due to an anisotropy field, the field pulse is applied in the y-direction. The resulting effective field, demagnetization field and motion of the magnetization are also indicated. The demagnetization field is responsible for the large angle rotation.

In order to achieve fast switching, both the field pulse and the anisotropy field must be large. The field pulse must be large to lift the magnetization out of the plane and to induce a strong demagnetization field. The anisotropy field has to be large in order to efficiently pin the magnetization to one of the stable configurations.

In order to simulate switch events, a uniaxial anisotropy has to be implemented in the model. A uniaxial anisotropy in the x-direction can be described by an anisotropy *field*, H_{ani}, in the y-direction. This anisotropy field tends to align the magnetization along the x-axis. The y-component of the effective magnetic field then becomes

$$H_y(t) = H_{pulse}(t) - \frac{2K}{\mu_0 M_s} m_y(t) = H_{pulse}(t) - H_{ani} m_y(t), \qquad (2.21)$$

with K the anisotropy constant. Equation (2.21) shows why the magnetization can rotate in the plane of the element over large angles. In the absence of an external bias field, only the anisotropy field can pin the magnetization along the x-axis. Just after excitation, the anisotropy field is very small, as it is proportional to m_y. The pinning of the magnetization is thus also small. Only when the magnetization approaches the y-axis, the anisotropy field becomes large. However, as the motion of the magnetization vector cannot be stopped instantaneously, the magnetization can cross the y-axis. At that point the energetically most favorable direction becomes the $-x$-direction and a complete switch is possible. When in the model H_{bias} = 0, H_{ani} = 0.4 kA/m and the 0.25 ns field pulse is used, the resulting motion of the magnetization is as shown in Figure 2.6. The magnetization reverses from m_x = 1 to m_x = −1, but shows also ringing, oscillations around the final equilibrium direction that increase the switching time.

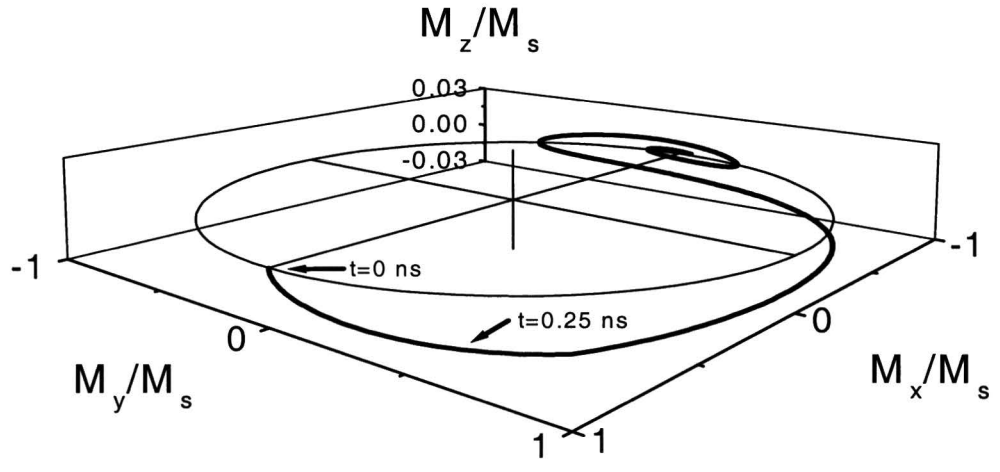

Figure 2.6: Simulated precessional switch of the magnetization vector from m_x=1 to m_x= −1. A number of oscillations (ringing) around the final equilibrium direction can be seen, making this switch slower than theoretically possible (ballistic). The field pulse duration is 0.25 ns and the amplitude is 0.8 kA/m. An anisotropy field of 0.4 kA/m in the y-direction is included in order to achieve two stable equilibrium directions. The bias field is set to 0 kA/m.

A switch at the ultimate switching time (half the precession period) is called a ballistic switch. In order to achieve a ballistic switch, the field pulse must have a particular amplitude and shape for a certain anisotropy field [9]. At the moment the magnetization is reversed, the field pulse must end, leaving the magnetization at $m_x = -1$ without introducing ringing.

2.5 Coupling effects in micromagnetic structures

So far, we have discussed only the response of a macrospin to magnetic field pulses. In real systems, however, it depends on the material and shape of the magnetic element in question as well as the presence of additional magnetic layers, whether or not the magnetic element will behave as a single macrospin. When the magnetization dynamics in a magnetic element is not uniform, the LLG-equation is only locally applicable to describe the magnetization dynamics. The magnetic element must then be divided into small regions that do act as a macrospin. Each region can then be separately described by the LLG-equation. If the magnetization direction is different in two neighboring regions, an additional term has to be included in the effective field in the LLG-equation of each region. This is the exchange field, the field due to the interaction that is responsible for the parallel alignment of spins in a ferromagnet. It is also responsible for spin wave generation in small magnetic elements. In this section we will discuss the effects that cause non-uniform spin dynamics.

A non-uniform magnetization in an element will arise when the effective magnetic field in an element is a function of position. The most important source of an inhomogeneous effective field is the demagnetization field at the edges of the element. At these edges, the spins feel a different internal field than spins in the center of the element, since at the edge the dipole field from the missing spins is absent, as shown in Figure 2.7a. This missing dipole field changes the internal field and this change can be described by a demagnetization field. It causes the domain formation in small magnetic elements in the absence of an external bias field.

In the presence of an external bias field, the element acquires a global magnetization and the effect of the missing dipole field is different at edges parallel and perpendicular to the magnetization in the element, indicated in Figure 2.7a by edge 1 and edge 2 resp. At edge 1, the dipole field from the missing spins would be *anti-parallel* with the bias field. Therefore, the effective field will be higher then in the center of the element due to the absence of this dipole field. At the edge 2, the situation is opposite. In this case the dipole field from the missing spins would be *parallel* with the bias field. The effective field will thus be lower at these edges, compared with the center of the element.

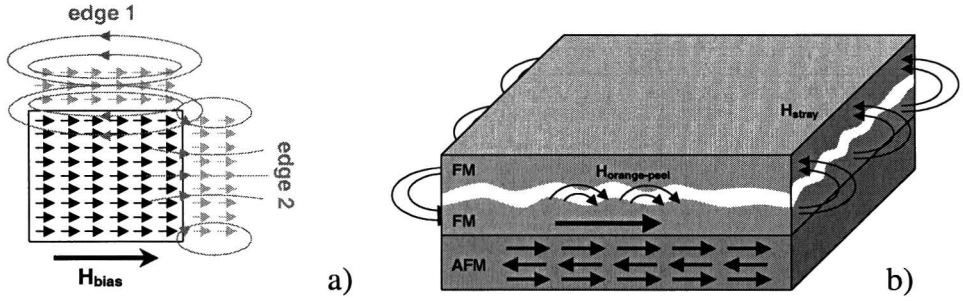

Figure 2.7: (a) A single magnetic layer in an external bias field. The missing spins and their dipole fields at the edges are drawn in gray. At edge 1 the dipole field is in anti-parallel alignment with the bias field, at edge 2 it is aligned parallel. (b) A typical magnetic tunnel junction stack consisting of an Anti-FerroMagnetic (AFM) layer and two FerroMagnetic (FM) layers, separated by a thin aluminum-oxide barrier. The direction of the orange peel-field and strayfield are indicated.

The influence of the missing dipole field is only significant in the region near the edge. In terms of magnetization dynamics, we have seen that the effective field determines the motion of the magnetization vector, and in particular the frequency. The precessional motion will thus have a different frequency near the edges compared with the center frequency. These different frequencies are called *edge modes*, since they manifest only near the edges of the element [13]. The precession with the center frequency is called the uniform mode, since it has the frequency all the spins would have in the absence of the edge effects.

The situation becomes more complicated if the magnetic element is part of a stack of magnetic layers, e.g. in case of a magnetic tunnel junction. Let us consider for example the magnetic tunnel junction shown in Figure 2.7b. The Anti-FerroMagnetic (AFM) layer induces *exchange biasing* in the lower ferromagnetic (FM) layer, which results in a large shift of the hysteresis loop of this FM layer towards positive field values, see Figure 2.8. The magnetization of this FM layer will not switch when small external magnetic fields are applied, hence this layer is called the *pinned* layer. The pinned and top FM layers are separated by a very thin aluminum-oxide layer. As the two FM layers are so close to each other, a coupling arises between them, which is called the *interlayer coupling*. The interlayer coupling between the two FM layers is position dependent and consists of the so-called *orange-peel* coupling and *strayfield* coupling.

The orange-peel coupling originates from the interface roughness between the FM layers and the aluminum-oxide barrier. Magnetic field lines from the pinned FM layer can penetrate the barrier and flow into the top FM layer. Due to these field lines the top layer couples ferromagnetically to the pinned FM layer and therefore also the hysteresis loop of the top FM layer is shifted to positive field values. This shift is less than the shift of the pinned FM layer.

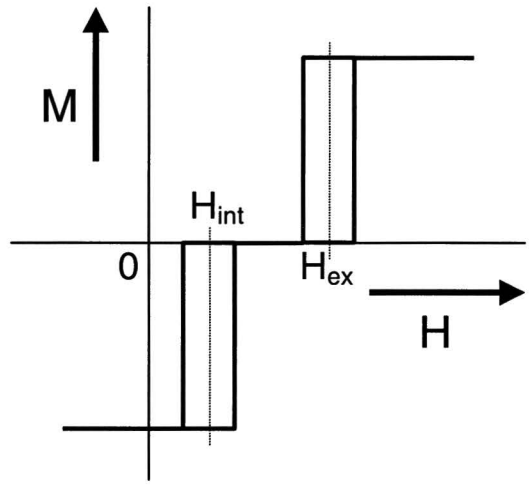

Figure 2.8: Schematic drawing of a hysteresis loop of the magnetic element sketched in Figure 2.7b. The exchange bias field and the interlayer coupling field are indicated. Both FM layers are assumed to be identical in size and material.

The strayfield coupling is the result of the magnetic field lines that point out from the edges of the pinned FM layer. These stray-fields have an opposite direction in the top FM layer compared to magnetization of the pinned FM layer. Therefore, the strayfield coupling is anti-ferromagnetic and is thus in competition with the orange-peel coupling. It is strongest at the edges of the top FM layer, see Figure 2.7b.

It is clear that the orange-peel field, strayfield and the demagnetization fields in combination with a possible external bias field, can give rise to a highly non-uniform internal effective field in a magnetic element. This uniform field allows for different spin modes, in particular localized edge modes, as we will show in discussing the experiments performed on real magnetic tunnel junction elements.

To conclude this chapter, we have explained the basics of precessional magnetization dynamics in small magnetic elements. We have presented some results from the numerical model and we will use them to analyze and discuss the observed dynamics in magnetic elements. These magnetic elements will be discussed in the next chapter, as well as the experimental techniques used to study them.

3 Experimental Setup

The investigation of magnetization dynamics was performed in this work on two different samples. Both contain small Py elements that were deposited on top of a current line. Short current pulses that are coupled into the current line induce a magnetic field pulse, which triggers a precessional motion of the magnetization vector in these elements. In order to detect this motion in the sub-nanosecond time domain, a pulsed optical setup was used that measured the magneto-optical Kerr effect versus time. A high aperture microscope objective was used to achieve a spatial resolution down to one micrometer and to perform measurements of two components of the magnetization vector.

In this chapter, first the studied magnetic samples will be presented in detail. The way in which magnetic field pulses were applied will be explained and issues concerning waveguide structures will be discussed. The main characteristics of the magnetic samples will be described and the layout of the structures will be shown. Next, the optical techniques used to study these magnetic samples will be discussed. The magneto-optical Kerr effect (MOKE) will be explained and the sensitivity of the effect will be deduced. The optical setup with a photo-elastic modulator that is used for static MOKE measurements will be presented. The implementation of an electrical-pump / optical-probe technique, which allowed time-resolved MOKE measurements, will be described and finally the extension of the setup to *vectorial* time-resolved MOKE will be presented.

3.1 Magnetic samples

The layout and structuring of magnetic samples is of critical importance for studying the fast magnetization dynamics in ferromagnetic metals. Magnetic field pulses with rise times much shorter than 1 ns are required to induce a precessional motion of the magnetization in magnetic materials. It is impossible to generate field pulses with such short rise times with Helmholtz coils, so other methods have been developed.

In almost all cases, the magnetic field pulse is induced by a current pulse that propagates through a thin metallic wire, on top of which magnetic material is deposited. From symmetry arguments, the induced magnetic field is perpendicular to the current line and at the center of the current line also in the sample plane. In order to achieve high fields, the current density has to be large, which implies that the dimensions of the current line have to be small. The magnitude of the induced field can be estimated from the approximate formula

$$H_{pulse} \simeq V/(2wZ), \tag{3.1}$$

where V is the applied voltage, Z the impedance of the current line and w the width of the signal line that carries the current. Another important aspect is that high frequency components of the current pulse must be able to propagate through the current line without significant losses, otherwise the rise and fall times of the pulse will not be sufficiently short.

These two considerations lead to a so-called microscopic coplanar waveguide design. Such a waveguide usually consists of a signal line with two ground plates on each side. The waveguide is terminated with a 50 Ω resistance at one end to minimize reflections of high frequency components of the signal. The width of the signal line and the distance between the central line and the ground plates are chosen in such a way, that in combination with the dielectric constant of the substrate the impedance of the waveguide is matched to 50 Ω. The current pulse can be generated by photoconductive switches [14], but also with commercial pulse generators [15].

In this work, a commercial AVTECH AVN-1-C-P pulse generator was used that can produce voltage pulses with a minimum rise time of 100 ps. The pulse shape can be changed by varying the rising (Tr) and falling (Tf) edge settings of the pulse generator. This way, pulse lengths can be produced between 0.2 and 1.5 ns, although in some cases there is a significant amount of after-pulsing present. This means that the pulse profile is not flat after the main pulse but contains some lower amplitude peaks. Screen shots from a 12.5 GHz sampling oscilloscope are depicted in Figure 3.1 for two settings mostly used in this work. The figures show the rise and fall times, the pulse length and the presence of after-pulsing. The repetition rate of the pulses can be set from 50 to 260 MHz and also synchronized with a pulsed laser system via a trigger input channel.

This pulse generator was used to induce magnetic field pulses in two different samples. The layout, structure and contacting of these sample will be discussed below.

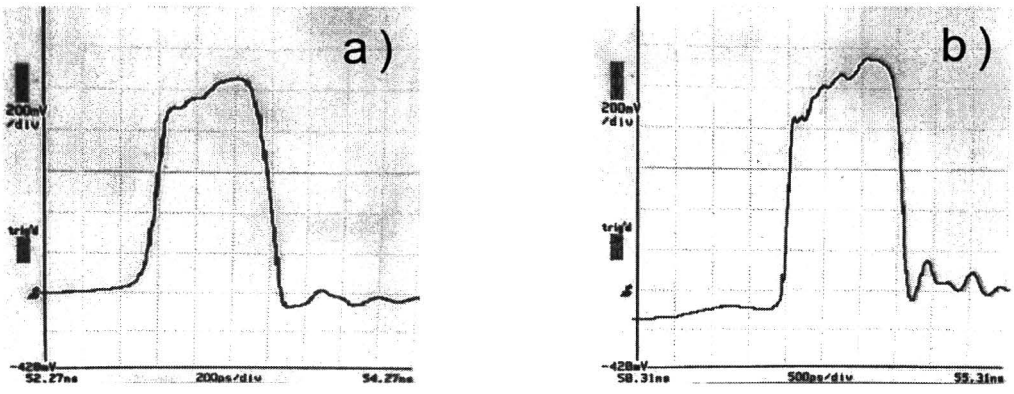

Figure 3.1: Screenshots from a 12.5 GHz sampling oscilloscope showing the voltage pulse profiles of two settings of the pulse generator. (a) Profile of a 0.6 ns pulse with settings Tr=2, Tf=6. (b) Profile of a 1.5 ns pulse with settings Tr=5, Tf=8.

3.1.1 Circular Py dots on a coplanar waveguide

The first sample used in this work is schematically drawn in Figure 3.2. It consists of a GaAs wafer, on top of which a microscopic coplanar waveguide structure was deposited, with Au striplines of 200 nm thickness and 50 μm width. The distance between the center of the lines is 150 μm. The striplines were covered with an insulating layer of SiN_x to prevent a current flow through the magnetic elements, which were grown with Molecular Beam Epitaxy (MBE) on top of this SiN_x layer. These magnetic elements consist of Permalloy ($Ni_{81}Fe_{19}$) dots of 30 nm thickness, with diameters varying from 4 to 50 μm. Different lines contain Py dots with different diameter. At the sample edges, the striplines were not covered with the insulating layer and there the striplines could be connected to the pulse generator.

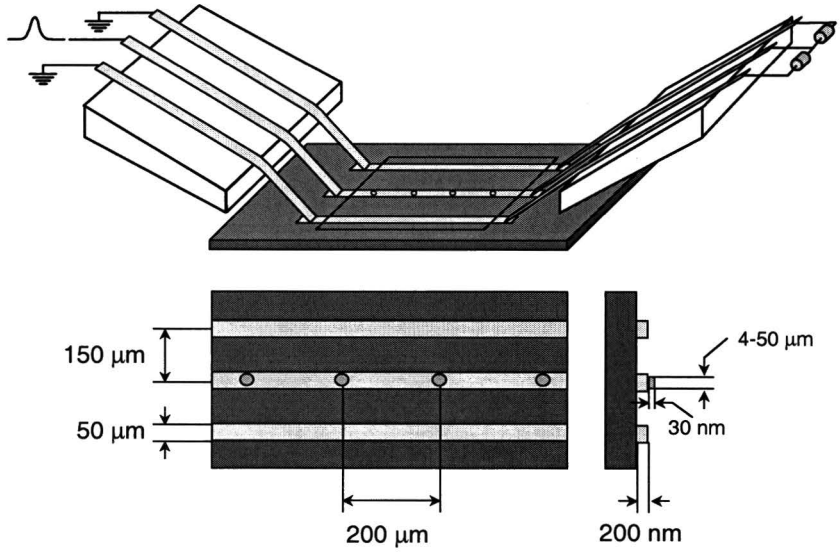

Figure 3.2: Schematic layout of the contacting and structure of sample A. The relevant dimensions of the gold line and the Py dots are indicated.

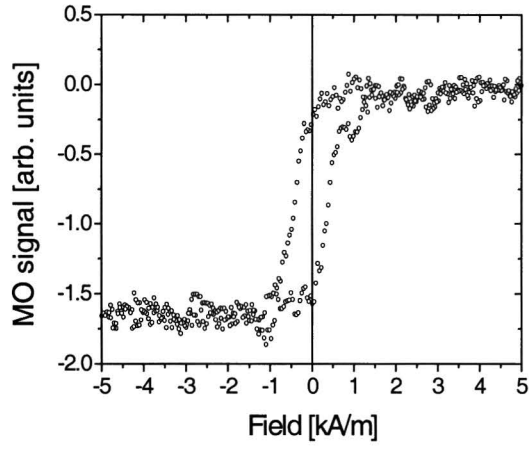

Figure 3.3: In-plane easy axis hysteresis loop obtained with a static MOKE experiment on a circular Py dot of diameter 30 μm. This hysteresis loop shows a coercivity of 0.4 kA/m.

To minimize the impedance mismatch of the pulse generator and the sample at high frequencies, three striplines were terminated with resistors, see Figure 3.2. The connectors at both ends of the sample can be lifted upwards to connect current lines with magnetic dots of different size. This way, experiments are possible on a large variety of Py dots. The pulse generator has an output impedance of 50 Ω, whereas the dc resistance of the sample (stripline- and contact-resistance) was 114 Ω. This results in severe amplitude decrease for frequencies above ~5 GHz. Nevertheless, with this setup current pulses with a rise time of 200 ps could be sent through the striplines, fast and strong enough to induce precessional motion of the magnetization. An upper limit of the field pulse strength can be estimated with equation (3.1). With V = 5 Volt, w = 50 μm and assuming Z = 114 Ω, one obtains H_{pulse} = 0.4 kA/m.

In this work, the magnetization dynamics in Py elements with diameter 30 μm has been studied. This diameter is chosen from practical point of view, since these elements were deposited on one of the first gold lines, which allowed for fast positioning of the laser focus on one of the dots on that line. The magnetic properties of this Py element are determined by measuring the static hysteresis loops, shown in Figure 3.3. This measurement shows a coercivity of 0.4 kA/m. Since this is a circular dot, no uniaxial anisotropy is expected in the plane of the dot and therefore no preferential direction of the magnetization. Further in this Thesis, we will refer to this sample as "sample A".

3.1.2 Rectangular magnetic tunnel junctions on a current line

The second set of samples consists of a more complicated layer structure and is shown in Figure 3.4. It was grown and structured at Philips Research Laboratories. On top of a silicon/silicon-oxide substrate, a copper layer was deposited and patterned into a large number of copper structures by means of conventional liftoff techniques. These structures consist of two contact electrodes of dimensions 100 x 400 μm, interconnected by a

copper line with a width of 25 μm. The thickness of the copper structure was chosen to match the dc resistance of the lines as close to 50 Ω as possible. At the center of the copper lines, a pile of several layers was grown to form a magnetic tunnel junction. First, a Ta layer and a Py layer were deposited that act as seed layers to assure good growth of subsequent layers. The first one of these is an anti-ferromagnetic IrMn (10 nm) layer that forms with a CoFe (5 nm) layer an exchange biased pinned magnetic layer. A thin layer of aluminum-oxide acts as a tunnel barrier between the CoFe and a NiFe (5nm) layer (the soft free magnetic layer). The whole stack was covered with Ta (3.5 nm) as a capping layer to prevent oxidation of the magnetic layer. The lateral dimensions of these tunnel junctions vary from 9 x 70 μm^2 to 5 x 5 μm^2. After deposition the exchange bias was in the direction perpendicular to the current line, thus in the same direction as a current induced magnetic field pulse.

In the original design of this sample, two copper electrodes on top of the junction were also included to be able to perform four-point electrical measurements [16]. In order to have optical access to the free magnetic layer, these top electrodes were in our case omitted and the Ta forms the top layer. . The large contact electrodes are also covered with the layers used for the magnetic tunnel junctions. Due to this additional amount of magnetic material, the total magnetic moment of the sample is enough to perform SQUID measurements.

The connectors of sample A could not be used in combination with a microscope objective, due to the small focal distance. Therefore, a different method of connecting the pulse generator to the sample was made.

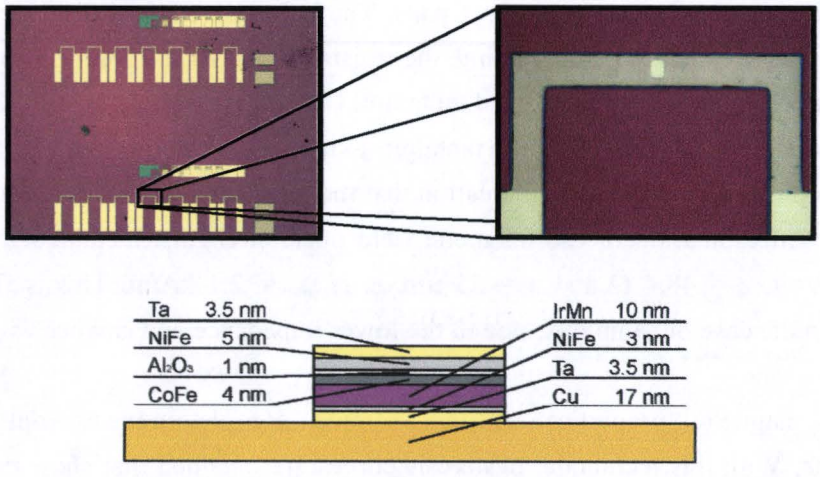

Figure 3.4: The layout and structuring of sample B. The top part shows microscope pictures of magnification 2.5 (a) and 50 (b). The contact electrodes, copper line and magnetic element can be clearly seen. The magnetic element has dimensions 9 x 13 μm. The bottom part shows the layers of which the magnetic element consists, including their thickness.

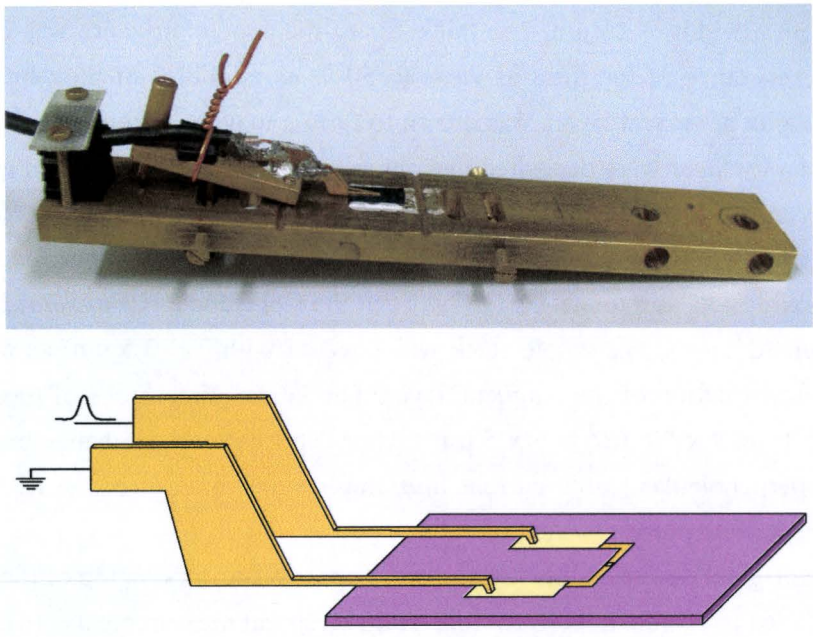

Figure 3.5: The contacting of sample B that is optically accessible with a microscope objective. The top part shows a picture of the sample holder, in which the sample, contacting elements and coax cable can be seen. The bottom part shows a schematic drawing of the contacting pads and the sample structure.

As shown in Figure 3.5, two stiff copper wires with pins at the end are pressed on the two copper contact pads of a particular junction, while keeping the wires as parallel to the sample surface as possible. These wires are soldered on larger electrodes that are connected to a coax cable. This configuration is not a waveguide structure, but nevertheless it proved to be possible to send short current pulses through the wires. In this case, the dc resistance could be set almost exactly to 50 Ω by choosing the proper position of the pins on the copper contact pads. The influence of the extra layers on the contact pads was such that after contacting, the resistance was of the order of several MΩ due to the tunnel barrier and the oxidized tantalum. However, by applying a dc voltage of a few Volts, dielectric breakdown of the tantalum-oxide and aluminum-oxide resulted in a resistance drop down to 48.4 Ω, an indication that the interface resistance was reduced to almost zero. An estimation of the magnetic field pulse strength, calculated from (3.1) with V = 5 Volt, Z = 48.4 Ω and w = 25 μm, is H_{pulse} = 2.1 kA/m. This is five times higher than in the case of sample A, due to the lower impedance and smaller width of the current line.

The magnetic properties of this sample are determined from SQUID measurements. With this technique, hysteresis curves are obtained that show the pinned and the free layer as in Figure 3.6a. The CoFe layer is strongly exchanged biased with the anti-ferromagnetic layer, with an exchange bias field of H_{ex} = 22 kA/m. The "free" NiFe layer is clearly coupled to the CoFe layer, as the switching fields are shifted to positive field values. The interlayer coupling field is, however, much smaller than the exchange bias field, H_{int} = 2.4 kA/m. The coercivity of the free layer is determined to be 0.7 kA/m.

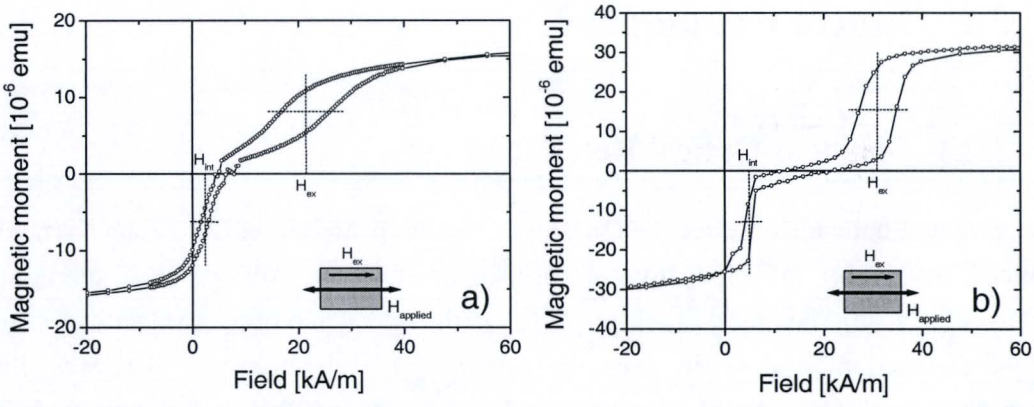

Figure 3.6: SQUID measurements of the magnetic layers of sample B. (a) Hysteresis loop before annealing. The pinned and free layer are visible, but the switching fields are not well defined. (b) Hysteresis loop after annealing of the sample, but without rotating the exchange bias direction. The pinned and free layer are well separated, the switching fields are much more defined and the remanence is increased. The magnetic moment is different since these measurements were performed on different sample pieces.

As mentioned before, the exchange bias direction was initially in the direction of the field pulse, and consequently the direction of the interlayer coupling to the free layer as well. In order to excite the magnetization of the free layer, there has to be an angle between the magnetization and the field pulse, preferably 90°, since this yields a maximum torque. In principle this can be done by applying an external bias field that compensates for the interlayer coupling field and also rotates the magnetization 90°. However, a much nicer way to do this is to rotate the exchange bias direction in the plane with 90°. This can be done by annealing the sample above the blocking temperature of the anti-ferromagnetic layer and letting it cool down in an external magnetic field in the preferred direction. Moreover, annealing the sample improves the quality of the layers and the interfaces. This can be seen in Figure 3.6b, which shows a SQUID measurement of an annealed sample in which the exchange bias direction was not rotated. The switching regime of the free and pinned layer is well separated and the switching fields are much better defined. The exchange field H_{ex} has increased to 31 kA/m and the interlayer coupling field H_{int} to 5.0 kA/m. The coercivity of the free layer is reduced to 0.5 kA/m.

In this work, a magnetic element of dimensions 13 x 9 μm^2 has been studied because, as the sample was fixed on the sample holder, only seven elements could be accessed electrically (see Figure 3.4). Three of these seven elements had dimensions 13 x 9 μm^2, so we started with investigating one of these elements to spare the other ones for example in case the current line would be overloaded. We will refer to this sample as "sample B".

3.2 Optical techniques

3.2.1 Magneto-Optical Kerr Effect

The magneto-optical Kerr effect (MOKE) was first discovered in 1877 by John Kerr, who noticed that light, reflected from a magnetized surface, experiences a change in polarization state. The origin of this effect lies in the interaction of photons with electrons in the conduction band of the magnetic material. Optical selections rules only allow transitions for which $\Delta l = 1$ and $\Delta m = \pm 1$, with l the orbital and m the magnetic quantum number of the electrons. The photons thus couple to the orbital angular momentum of the electrons. Due to the spin-orbit interaction, the orbital angular momentum of the electrons $\vec{L}$ is correlated to their spin angular momentum $\vec{S}$. One is thus able to probe the spin system via the optical selection rules on orbital angular momentum. In ferromagnetic transition metals, which we will study in this work, the orbital angular momentum $\vec{L}$ of the electrons is significantly quenched. Therefore, the magneto-optical effect is very small, however, it is still measurable.

In MOKE experiments, a laser beam of known linear polarization is used. When this beam is incident on a magnetized sample, the MO Kerr effect results in a change of the polarization angle and an increased ellipticity. This can be understood when linear polarized light is viewed as a combination of left- and right-handed circularly polarized light. An electron spin imbalance, present in a magnetized sample, will lead to different absorption rates and phase shifts for left- and right-handed circularly polarized light, when reflected from the surface. Consequently, the polarization state of the laser beam is not conserved. The magnitude of the Kerr-effect is proportional to the magnetization of the sample. In non-magnetic metals, where there is no difference between the electronic band structure of spin-up and spin-down electrons, no MO Kerr effect is present.

Based on the geometry of the optical configuration, three types of the Kerr effect can be distinguished. They are defined depending on the orientation of the magnetization with respect to the sample plane respectively the plane of incidence of the laser beam, see Figure 3.7: the *longitudinal* Kerr-effect, the *transversal* Kerr-effect and the *polar* Kerr-effect. The magnitude of the Kerr-effect is different in each case. The two main parameters that determine the magnitude are the angle of incidence of the linearly polarized laser beam and its polarization state with respect to the plane of incidence. The polarization can be parallel (p) or perpendicular (s) to the plane of incidence. Since the transversal Kerr-effect is much smaller than the longitudinal and polar Kerr-effect, it will not be considered in this work. We will calculate the magnitude of the MO Kerr-effect in the longitudinal and polar geometry, for the case of a magnetic layer with a thickness much larger than the penetration depth of light.

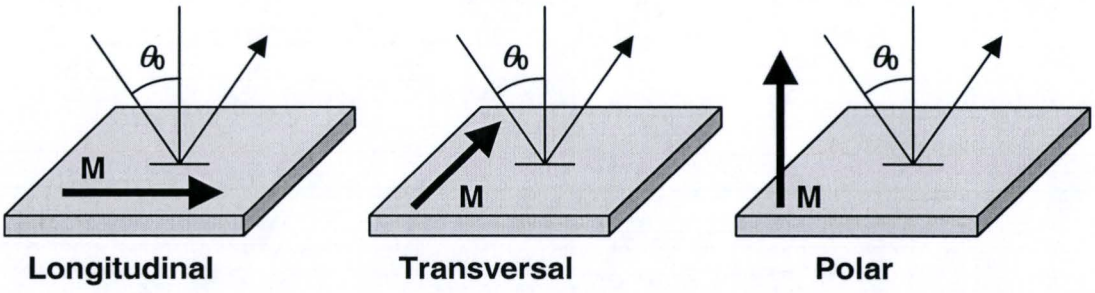

Figure 3.7: The three different Kerr-geometries depending on the orientation of the magnetization of the magnetic element with respect to the element surface and the plane of incidence of the laser beam. Only the longitudinal and polar geometry are considered in this work.

Starting with a magnetization dependent dielectric tensor and solving the Maxwell equations for the case of a reflection from a single magnetized surface [17], the polarization state of the reflected light beam is given as follows:

$$\begin{pmatrix} E_p \\ E_s \end{pmatrix} = \begin{pmatrix} r_{pp} & r_{ps} \\ r_{sp} & r_{ss} \end{pmatrix} \begin{pmatrix} E_{p0} \\ E_{s0} \end{pmatrix}, \tag{3.2}$$

where r_{ij} are the elements of the Fresnel reflection matrix and represent the ratios of the incident j polarized electric field (E_{j0}) and the reflected i polarized electric field (E_j). These elements can be expressed as

$$\begin{aligned} r_{pp} &= \frac{n_1 \cos\theta_0 - n_0 \cos\theta_1}{n_1 \cos\theta_0 + n_0 \cos\theta_1} - i \frac{2 n_0 n_1 \cos\theta_0 \sin\theta_1 m_x Q}{n_1 \cos\theta_0 + n_0 \cos\theta_1} \\ r_{ps} &= i \frac{n_0 n_1 \cos\theta_0 \left(m_z \cos\theta_1 - m_y \sin\theta_1 \right) Q}{\left(n_1 \cos\theta_0 + n_0 \cos\theta_1 \right)\left(n_0 \cos\theta_0 + n_1 \cos\theta_1 \right)\cos\theta_1} \\ r_{sp} &= i \frac{n_0 n_1 \cos\theta_0 \left(m_z \cos\theta_1 + m_y \sin\theta_1 \right) Q}{\left(n_1 \cos\theta_0 + n_0 \cos\theta_1 \right)\left(n_0 \cos\theta_0 + n_1 \cos\theta_1 \right)\cos\theta_1} \\ r_{ss} &= \frac{n_0 \cos\theta_0 - n_1 \cos\theta_1}{n_0 \cos\theta_0 + n_1 \cos\theta_1} \end{aligned}, \tag{3.3}$$

with the complex refraction indices n_0 and n_1 at the air-sample interface and the incident angle θ_0 and complex refracted angle θ_1. m_x, m_y and m_z are the components of the magnetization vector (normalized to M_s) and Q is a complex constant that represents the strength of the magneto-optical effect.

The Kerr rotation θ_K and ellipticity ε_K can be expressed in terms of these matrix elements in the following way:

$$\begin{aligned} \theta_K^p + i\varepsilon_K^p &= r_{sp} / r_{pp} \\ \theta_K^s + i\varepsilon_K^s &= r_{ps} / r_{ss} \end{aligned}. \tag{3.4}$$

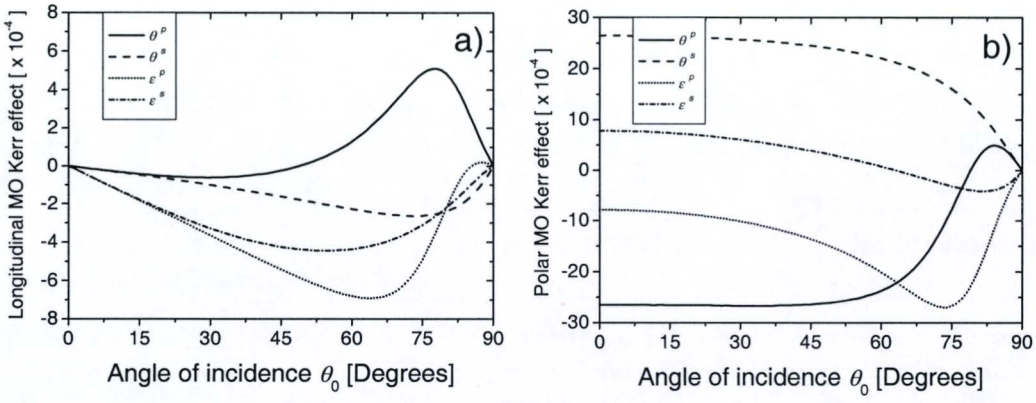

Figure 3.8: The MO Kerr rotation and ellipticity as a function of angle of incidence for the longitudinal (a) and polar (b) geometry. The rotation and ellipticity are calculated for both s and p polarized light for the case of Permalloy and λ=600 nm.

With the use of Snell's law, θ_1 in equation (3.3) can be eliminated. The Kerr rotation and ellipticity can then be calculated as a function of angle of incidence. The material parameters n and Q depend on the wavelength of the laser beam. For the case of Permalloy, for which $n = 1.96 - 3.3i$ and $Q = 0.0079 + 0.0076i$ if $\lambda_{laser} = 600$ nm [18], the result for each polarization state is shown in Figure 3.8 for the polar geometry ($m_z = 1$) and longitudinal geometry ($m_y = 1$). It is important to note that the polar Kerr effect is on average an order of magnitude higher than the longitudinal Kerr effect. In case of in-plane magnetization, the change in ellipticity is much larger than the change in rotation at low angles of incidence. Furthermore, the polarization change of the reflected laser beam from a Py surface with respect to the incident beam is very small, so sensitive modulation schemes are absolutely necessary to detect this effect.

There exist also a corresponding MO-effect for a configuration with transmitted light. Light transmitted through a magnetized medium (or passing through a region with a magnetic field) experiences a change in rotation. This effect is called the Faraday-effect and can influence Kerr-rotation measurements, for example when transparent optical components (microscope objective) are placed close to the sample in the magnetic field. In all experiments performed the Faraday-effect had no influence on the measurement signal, or was accounted for.

3.2.2 Static MOKE

Static MOKE is the technique for measuring the magnetization of a sample as function of an applied magnetic field. The change in magnetization is detected by measuring the MO Kerr ellipticity or rotation. For our static MOKE measurements the following optical setup was used. A weak laser beam, reflected from a beam splitter from the output of a Ti-sapphire 82 MHz pulsed laser, is sent through a polarizer with its polarizing axis 45° with respect to the fast axis of the bi-refringent crystal of a Photo-Elastic Modulator

(PEM). This beam is directed off axis into a high aperture lens, that focuses the laser beam on the sample, see Figure 3.9. Due to this off-axis entrance, the angle of incidence, θ_0, of the laser beam with the normal of the sample plane is non-zero. The setup is then sensitive to in-plane magnetization, however only with limited sensitivity, see Figure 3.8. The reflected light is picked up with a mirror and directed through an analyzer to a Si-photodiode that serves as a detector.

The photo-elastic modulator changes the polarization state of the laser light from left to right circular polarization by mechanically compressing the bi-refringent crystal. The frequency of this compression is 50 kHz, which is also the reference signal for a lock-in amplifier. It turns out that from the 1f (50 kHz) and the 2f (100 kHz) signal on the lock-in amplifier, the Kerr-ellipticity respectively the Kerr-rotation can be calculated, according to

$$\begin{aligned} \varepsilon_K &= \frac{1}{2\sqrt{2}J_1(A)}\frac{V_{1f}}{V_{dc}} \\ \theta_K &= \frac{1}{2\sqrt{2}J_2(A)}\frac{V_{2f}}{V_{dc}} \end{aligned} \quad . \tag{3.5}$$

Here, J_n is the n-th order Bessel function and A the maximum retardation of the PEM. A detailed derivation of these 1f- and 2f-signals, using the Jones calculus, can be found in [19]. The PEM thus allows for the detection of the very small changes in rotation and ellipticity by means of phase sensitive detection. The Kerr ellipticity and rotation are both linearly proportional to the magnetization, so from both signals parameters like the switching field(s) of the magnetic layer(s) can be easily extracted. Calibration of the signals to get magnetization values relative to M_s is also possible when the full switching curve is measured.

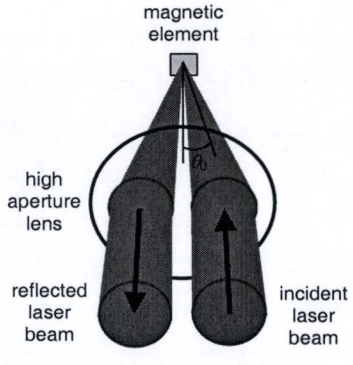

Figure 3.9: Schematic picture of an off-axis entrance of the incident laser beam into a high aperture lens. The angle of incidence, θ_0, is also shown.

The analyzer can be set with its polarizing axis parallel to the *p*- or to the *s*-direction of the reflected light. In most cases, aligning the analyzer parallel to the *p*-direction gives higher sensitivity.

The magnetic field that is used to switch the magnetization is produced by a pair of Helmholtz coils. These coils can generate a magnetic field up to approximately 14 kA/m. Hysteresis loops are obtained by sweeping the field from negative to positive values and back.

3.2.3 Time-resolved MOKE

In time-resolved MOKE (TR-MOKE) experiments, the dynamic response of the magnetization of a magnetic layer to an applied magnetic field is measured. The dynamics occur on nanosecond time-scales. In order to study such fast magnetization dynamics, a measurement setup based on a stroboscopic technique is used [20]. Magnetic field pulses are applied locally to a magnetic sample with the same repetition rate as a Ti-sapphire pulsed laser system. This laser system produces laser pulses of ~70 femtosecond duration with a repetition rate of 82 MHz. The output power is approximately 1 Watt and the wavelength of the light can be varied between 720 and 900 nm. The laser pulses arrive at the sample with a defined time delay after the magnetic pulse. This delay time can be varied by using a mechanical delay line that extends the optical path of the laser beam. Via the MO Kerr-effect, each reflected laser pulse then gives information on the magnetization at the time delay set by the momentary position of the delay line.

The complete optical and electrical setup is shown in Figure 3.10. A laser beam with a wavelength of λ = 760 nm is splitted from the main laser beam with a beam splitter, and has an intensity of 70 mW. This probe beam is directed into an optical delay line with a length of 30 cm that consists of three retro-reflectors. The probe beam thus travels four times through the delay line, so that the optical path can be extended with 1.20 m. The total time window that can be probed in this case is 4 ns (1.20 m / $3 \cdot 10^8$ m/s). This is roughly one third of the total time between two pulses (82 MHz ≡ 12.2 ns). The zero delay can be put into the time window of the delay line by choosing the proper length of the coax cable between the PIN-diode and the pulse generator. A coax cable of 1 meter corresponds roughly to 5 ns extra traveling time of the trigger signal. After the delay line, the polarization of the laser beam is set parallel to the plane of incidence, since that polarization state has the highest transmission when using a beam splitter.

The waist of the laser beam is increased with the use of a *beam expander* that consists of two positive lenses of different focal length. The lenses are arranged in such a way that their focal points coincide and the resulting width of the probe beam is increased with the ratio of the focal lengths of the two lenses, see Figure 3.10.

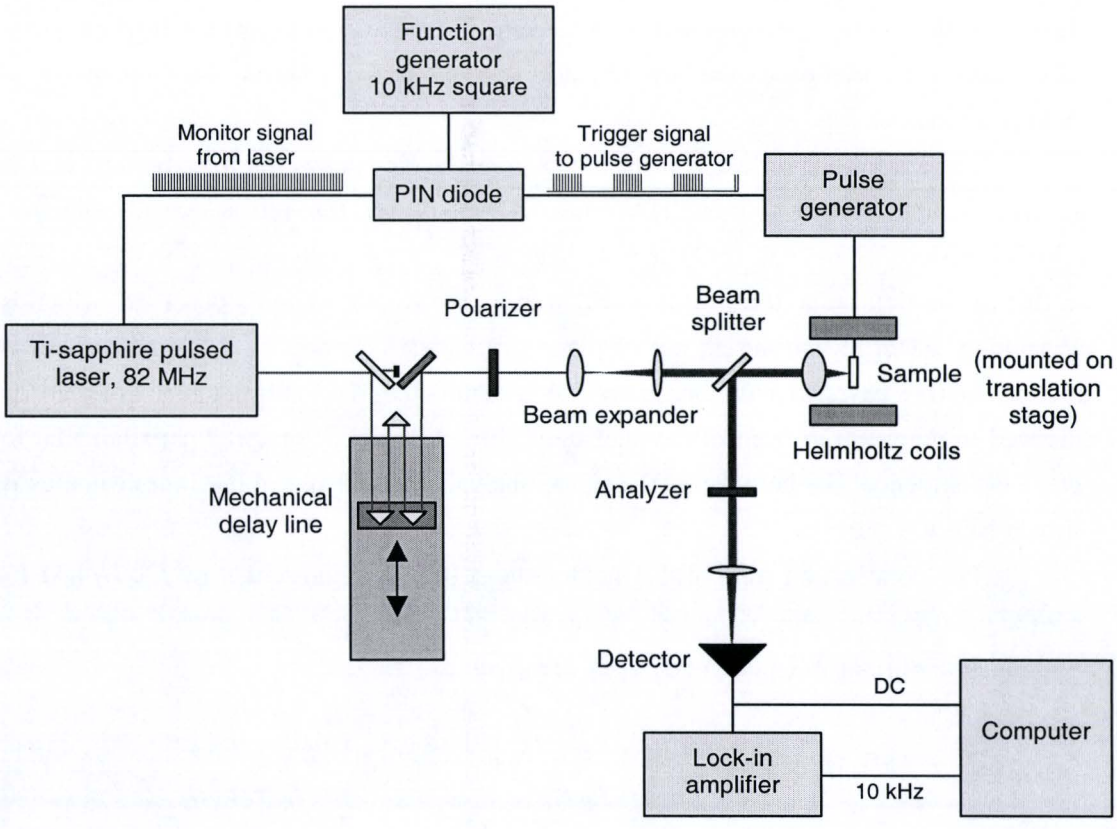

Figure 3.10: Schematic picture of the electrical-pump / optical probe setup to detect the magnetization dynamics induced by short magnetic field pulses.

This way, the large aperture of the lens that focuses the probe beam on the sample is used more efficiently, which gives a spot size closer to the theoretical minimum spot size and thus a higher spatial resolution.

Two different lenses were used to investigate the samples. A High Aperture Laser Objective (HALO) with a numerical aperture (NA) of 0.38 and focal length of 30 mm was used with sample A. This HALO can produce theoretically a diffraction limited spot of diameter d of 2.5 μm, according to the following formula [21].

$$d = \frac{1.27\lambda}{NA} \tag{3.6}$$

With sample B a microscope objective was used with a numerical aperture of 0.65. The distance between sample and objective was only ~1 mm. The theoretical diffraction limited spot size of the microscope objective is 1.5 μm. In both calculations, a laser wavelength of $\lambda = 760$ nm is used. The focused laser power on the sample is estimated to be of the order of 1 mW. Since the laser beam is focused on a few μm^2, the power density is of the order of 1 $mW/\mu m^2$, which will cause a local temperature rise of the sample of several tens of degrees. However, this increase in temperature occurs in a few ps, whereas the information carried by the reflected light is from the first few 100 fs. Therefore, it will

have no effect on the measurement, provided that a possible effect, which the heat pulse can have on the motion of the magnetization, is damped out before the next magnetic field pulse arrives.

The laser light reflected from the sample travels backwards into the lens and is splitted with the beam splitter. The reflected part passes through a second polarizer, which functions as an analyzer. The polarization axis of the analyzer is set to 45° relative to that of the first polarizer. In this configuration, the Kerr-rotation is observed, which is convenient when measuring an out of plane magnetization only, since the MO-effect is highest in this case. In case one wants to measure the Kerr-ellipticity, a λ/4-plate is inserted in the setup in front of the analyzer, with its slow axis oriented perpendicular to plane of incidence. For both cases, the signal analysis with the use of the Jones calculus is shown below.

The polarization state of the incident laser beam is represented by E_0. E_1 and E_2 are the polarization states of the laser beam after passing the optical elements, for the case without and with the λ/4-plate resp. They are given by

$$E_1 = M_{ana}^{45^\circ} M_{refl} E_0 = \begin{pmatrix} \frac{1}{2} & \frac{1}{2} \\ \frac{1}{2} & \frac{1}{2} \end{pmatrix} \begin{pmatrix} r_{pp} & r_{ps} \\ r_{sp} & r_{ss} \end{pmatrix} \begin{pmatrix} 1 \\ 0 \end{pmatrix} = \frac{1}{2r_{pp}} \begin{pmatrix} 1+\theta_K^p + i\varepsilon_K^p \\ 1+\theta_K^p + i\varepsilon_K^p \end{pmatrix}, \qquad (3.7)$$

$$E_2 = M_{ana}^{45^\circ} M_{\lambda/4}^{90^\circ} M_{refl} E_0 = \begin{pmatrix} \frac{1}{2} & \frac{1}{2} \\ \frac{1}{2} & \frac{1}{2} \end{pmatrix} \begin{pmatrix} 1 & 0 \\ 0 & i \end{pmatrix} \begin{pmatrix} r_{pp} & r_{ps} \\ r_{sp} & r_{ss} \end{pmatrix} \begin{pmatrix} 1 \\ 0 \end{pmatrix} = \frac{1}{2r_{pp}} \begin{pmatrix} 1-\varepsilon_K^p + i\theta_K^p \\ 1-\varepsilon_K^p + i\theta_K^p \end{pmatrix}. \qquad (3.8)$$

M_{refl}, $M_{\lambda/4}^{90^\circ}$ and $M_{ana}^{45^\circ}$ are the Jones matrices for reflection on the sample, the λ/4-plate and the analyzer resp. The intensity on the detector for both cases is

$$I_1 \sim |E_1|^2 = \frac{1}{\sqrt{2}r_{pp}} \left(1+2\theta_K^p + \left(\theta_K^p\right)^2 + \left(\varepsilon_K^p\right)^2\right) \cong \frac{1}{\sqrt{2}r_{pp}} \left(1+2\theta_K^p\right), \qquad (3.9)$$

$$I_2 \sim |E_2|^2 = \frac{1}{\sqrt{2}r_{pp}} \left(1-2\varepsilon_K^p + \left(\varepsilon_K^p\right)^2 + \left(\theta_K^p\right)^2\right) \cong \frac{1}{\sqrt{2}r_{pp}} \left(1-2\varepsilon_K^p\right). \qquad (3.10)$$

We see that the intensity contains a component due to the Kerr-rotation (no λ/4-plate) or the Kerr-ellipticity (with λ/4-plate).

These components are very small and in order to detect them, and to improve the signal-to-noise ratio, a modulation scheme is used. The 82 MHz monitor signal from the Ti-sapphire laser system, that functions as the trigger signal for the pulse generator, is sent through a PIN-diode, to which a 10 kHz square wave gate signal is supplied. The monitor signal is thus modulated with 10 kHz and as a result, the magnetic pulses that induce the fast magnetization dynamics are modulated into 10 kHz pulse trains, see Figure 3.10. The detector signal will then contain a 10 kHz component that is extracted

with the use of a Stanford Research Systems DSP lock-in amplifier. Signal-to-noise ratios up to 200:1 can be achieved this way. It is important to stress that the lock-in signal is linearly proportional to the *change* in rotation or ellipticity of the reflected probe beam due to the *output current* of the pulse generator. The intensity signal was measured simultaneously with the lock-in signal, by extracting the DC-signal with a low-pass filter.

The magnetic bias field in the horizontal direction of the sample plane is produced by the same pair of Helmholtz coils as in the static MOKE case. These coils were used to apply a bias field perpendicular to the current line when the magnetization dynamics in sample A was investigated. The magnetic field in the vertical in-plane direction is produced by a u-shaped electromagnet (omitted in Figure 3.10). The sample holder could be placed right between the two poles of the magnet. Bias fields perpendicular to the current line of sample B could be produced up to 8 kA/m. The magnetic field from this magnet is, however, expected to be less uniform then the field from the Helmholtz coils.

3.2.4 Vectorial TR-MOKE

The time-resolved magneto-optical technique explained in the previous section is only sensitive to the out-of-plane magnetization of the sample, since the polar geometry is used and the reflected light is collected by a single detecting element. In order to get a complete picture of the motion of the magnetization vector, also the in-plane components must be measured. Especially in the case of large angle excitations, the out-of-plane signal alone does not give enough information on the complete motion of the magnetization vector. In recent years, the out-of-plane component was measured by several experimental groups with the use of the Kerr-effect, while for detecting the in-plane components, different techniques have been developed. For example, the pure transverse Kerr-effect is used in [22] and magnetization induced second harmonic generation is used in combination with polar MOKE in [14], [23].

In this work, a method for detecting the in-plane components was developed that is similar to the method in [18] and is based on the following principle. Although the probe beam is incident perpendicular to the sample plane, due to the finite width of the beam some of the light will have an angle of incidence that is larger than 0° when it is focused with a high NA lens, as visualized in Figure 3.11. The average angle of incidence of the whole converging laser beam is, of course, 0° to the normal of the sample plane.

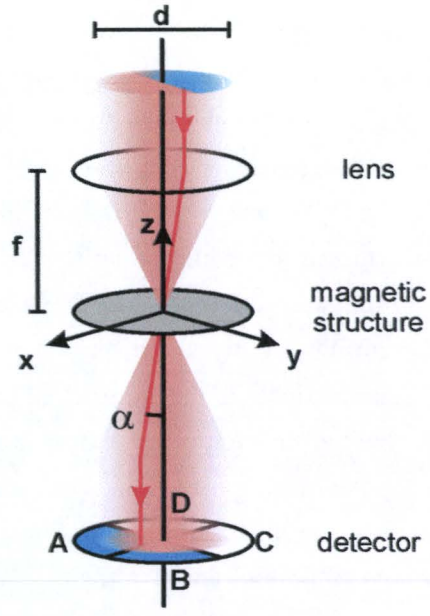

Figure 3.11: Geometry of the four-quadrant detection scheme. The reflected light from the magnetic structure is mirrored, in order to separate the incident and reflected laser beam. f is the focal length of the lens, d is the waist of the laser beam and α is the average angle of incidence for the dark part of beam.

Quadrant	Sensitive to
A	$K_l \cdot (M_x - M_y) + K_p \cdot M_z$
B	$K_l \cdot (M_x + M_y) + K_p \cdot M_z$
C	$K_l \cdot (-M_x + M_y) + K_p \cdot M_z$
D	$K_l \cdot (-M_x - M_y) + K_p \cdot M_z$
Magnetization components	Proportional to
M_x	(A+B) – (C+D)
M_y	(A+D) – (B+C)
M_z	A+B+C+D

Table 3.1: The components of the magnetization to which the quadrants are sensitive, with K_l and K_p the longitudinal and polar Kerr effect for a certain average angle of incidence resp. (top). The addition and subtracting rules to calculate the components of the magnetization (bottom).

Let us consider the average angle of incidence of the left half of the probe beam, as in Figure 3.11. With a microscope objective (NA 0.65) and assuming a uniform spherical laser beam, this angle is 15° degrees. This part of the probe beam is thus able to probe the in-plane magnetization in the $+x$-direction, as well as the out-of-plane magnetization ($+z$-direction). According to Figure 3.8, the Kerr-effect due a magnetization component in the x-direction is very different from the Kerr-effect due to a component in the z-direction. The same applies for the right half of the probe beam, which probes the magnetization in the $-x$-direction, as well as the out-of-plane magnetization ($+z$-direction). If the left and right parts of the reflected probe beam are detected separately, the difference of the signals will be proportional to the in-plane magnetization, while the sum of the signals will be proportional to the out-of-plane magnetization.

The above method can be extended for measuring three dimensions by considering four parts of the probe beam, also shown in Figure 3.11. The resulting analysis of the signals is shown in Table 3.1.

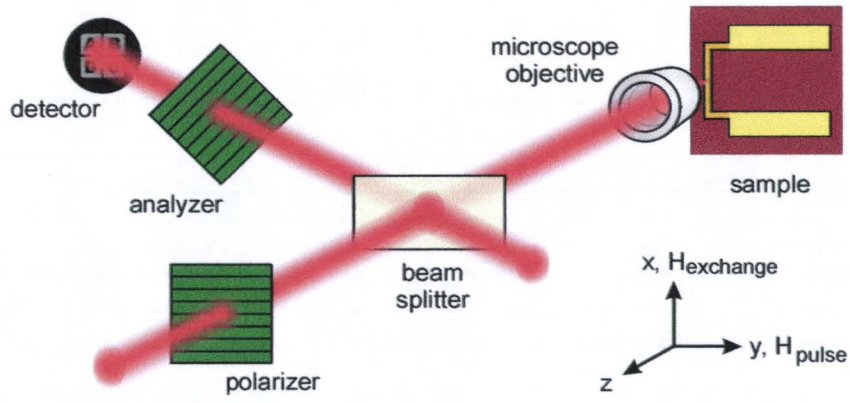

Figure 3.12: Three-dimensional view of the optical setup, which shows the main optical components needed to detect the magnetization dynamics.

For clarity, a three-dimensional view of the optical setup used with sample B is shown in Figure 3.12. The main optical components needed to detect all the components of the magnetization dynamics are indicated. The reflected light from the sample is focused on a four-quadrant detector, after passing through the analyzer. This way the Kerr-rotation (or Kerr-ellipticity in case a $\lambda/4$-plate is used) of the reflected laser beam is measured. As can be seen in Figure 3.8, in the longitudinal geometry the Kerr-ellipticity is much larger than the Kerr-rotation, in the case of layer thicknesses larger than the penetration depth of the laser light.

It will be clear that the alignment of the probe beam on the optical elements, especially with respect to the microscope objective and the four-quadrant detector, is of crucial importance to be able to use the addition and subtracting rules of Table 3.1. Misalignment of the probe beam into the microscope objective or onto the four-quadrant detector will destroy the symmetry between the four parts of the beam. As a result, the sensitivity to the in-plane magnetization of the four parts of the probe beam changes, since the average probe angle will change. In practice, however, these problems can be well handled. When the alignment is good, the calculated signals for the *x*-, *y*- and *z*-component of the magnetization will have only some minor crosstalk, after using the sum and difference rules of the detector signals according to Table 3.1. If the laser beam is put on the quadrant detector in such a way that the DC power on the quadrants is the same, any crosstalk present will then be caused by a misalignment of the incident laser beam on the microscope objective. We can correct for the crosstalk afterwards, by demanding that the phase difference between, for example the *y*- and *z*-direction, has to be close to 90° when a precessional motion is observed. This can be accomplished by multiplying the signals A, B, C and D with correction factors. The total (A+B+C+D) signal amplitude has to be preserved, otherwise it will affect the M_z-measurement. The correction procedure has thus the effect of setting the sensitivity to the in-plane magnetization of all the quadrants equal. This way, the measurement data can be corrected for any small misalignment present in the setup.

Quadrant	Sensitive to	Magnetization components	Proportional to
A	$-K_{l1} \cdot M_y + K_p \cdot M_z$	M_y	$c_A \cdot A - c_B \cdot B$
B	$+K_{l2} \cdot M_y + K_p \cdot M_z$	M_z	$c_A \cdot A + c_B \cdot B$

Table 3.2: Adding and subtracting rules in the case when measuring with two quadrants, and allowing for some crosstalk. K_{l1} and K_{l2} are the longitudinal Kerr effect for different average angle of incidence resp. (top). c_A and c_B are the correction factors needed to correct for the crosstalk (bottom).

In this work, the laser beam was focused on two quadrants, instead of four, since the detection scheme and alignment of the optical components was much easier this way. Moreover, with high bias fields in the x-direction, the precession amplitude will be small, and the change in M_x will be much smaller than the change in M_y. Therefore, the four-quadrant detector was aligned such that M_y and M_z were measured. Adding and subtracting the resulting lock-in signals gives in this case the magnetization components as shown in Table 3.2. The correction procedure is performed with two correction factors for each quadrant (c_A and c_B), in order to set the sensitivity K_{l1} and K_{l2} in Table 3.2 equal. Furthermore, whenever the magnitude of the magnetization vector is constant and equal to M_s, measuring two of the three components is sufficient to construct the total magnetization vector.

The calibration of M_y and M_z to obtain values relative to M_s was done in the case of sample A in the following way. With a 10 kHz square wave from a function generator, an alternating current was supplied to an external coil that induced magnetic fields in the $+y$- and $-y$-direction. Two quadrants of the detector were used to detect the in-plane variation of the magnetization. Above certain magnetic field strengths, full switching was achieved which yielded the maximum signal on the lock-in amplifier. This value was used to calibrate the M_y-measurements in the time-resolved experiments. With the now calibrated M_y-data as reference, the numerical LLG-model was used to calculate the amplitude of M_z oscillation. This way, also the M_z-data could be normalized to M_s.

In the case of sample B, the current line itself was used to produce the in-plane alternating magnetic field with a 10 kHz square wave. In order to achieve switching, an external bias field had to be applied to compensate for the interlayer coupling field. Again, at full switching the lock-in amplifier yielded the maximum signal, which was then used to calibrate the time-resolved data. The calibration of M_z was again done with the use of the numerical LLG-model.

4 Results

This chapter will discus the main results of the measurements that have been performed on the two magnetic samples with the experimental setup described in the previous chapter. First, the measurement data will be presented that successfully demonstrates the vector-resolved TR-MOKE setup. Vectorial measurements with different magnetic field pulses will be discussed and compared with simulations from the LLG-model. It will also be shown how these data can be used to extract the exact magnetic field pulse profile. Next, we will focus on the bias field dependence of the precessional frequency. The Gilbert damping parameter of the Py layer in the two samples will also be briefly addressed. Large angle excitations of the magnetization in sample B will be presented and discussed in detail. This chapter will conclude with a study of the spatial dependence of the magnetization dynamics. It will be shown that different edge modes coexist in the sample, which can be attributed to the interaction of different local magnetic fields with the spins near the edge of the sample. Finally we will show how the dynamic response of the magnetization in a magnetic element can give information about the static domain pattern in the element.

4.1 Demonstration of the vectorial TR-MOKE setup

Sample A

Vectorial measurements of the magnetization have first been carried out with sample A, using the HALO to focus the laser beam. In order to increase the light intensity on the detector, the probe beam was sent off-axis into the HALO and the reflected beam was picked up in its full intensity by a mirror, which replaced the beam splitter. A $\lambda/4$-plate was used to detect the changes in ellipticity, since the signal for the in-plane magnetization proved much higher than for the case of rotation. This is in agreement with Figure 3.8 from the previous chapter.

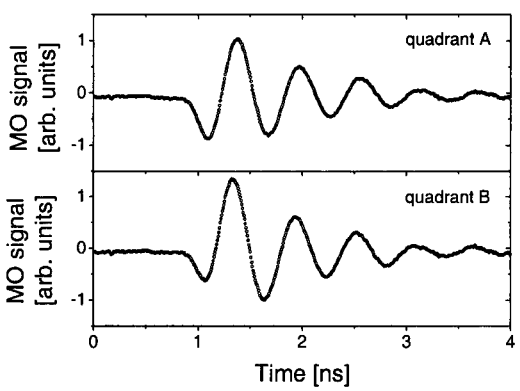

Figure 4.1: Raw lock-in data from two quadrants of the detector, normalized to the dc voltage on the detector. Pulse settings are Tr=2 and Tf=6, $t_{pulse} \cong 0.6$ ns, H_{bias}=2.4 kA/m along the x-axis.

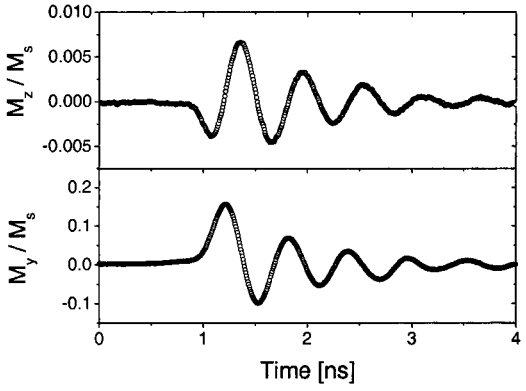

Figure 4.2: M_y and M_z calibrated to M_s, extracted from the raw lock-in data of Figure 4.1.

Figure 4.1 shows the raw data from the two lock-in amplifiers after applying voltage pulses of ~0.6 ns. The bias field in this case is 2.4 kA/m, large enough to saturate the magnetization along the *x*-axis, except perhaps at the edges of the dot. The laser spot is focused on the central region of the dot with a spot size of ~6 μm. It can already be seen that the signals from the two quadrant are different, an indication that they contain different components.

Before adding and subtracting these signals, an amplitude correction to the raw data was carried out in order to remove the crosstalk between the quadrants, as explained in section 3.2.4. The correction factors needed were c_A = 0.95 and c_B = 1.05, which indicates that the alignment of the optical components was satisfactory. It must be noted that these correction factors had to be changed only if the alignment of some of the optical components was changed. The added and subtracted data, after phase correction and calibration, are shown in Figure 4.2. From this figure, we see that subtracting the signals efficiently removes all correlated noise between the two quadrants, and as a result, the m_y data contains only very low noise. From the calibration procedure described in section 3.2.4 the sensitivities to m_y and m_z could be calculated. The ratio between the sensitivity to m_z and m_y was 90:1. As the amplitude of the m_y-oscillation is roughly 22 times larger than the amplitude of the m_z-oscillation, the M_z-signal is dominant in Figure 4.1. The contribution of the M_y-signal can, however, still be seen. This large difference in amplitude means that the precessional motion is indeed strongly elliptical, as expected from the simulations.

When the out-of-plane data is plotted versus the in-plane data, as in Figure 4.3, the excitation and relaxation of the magnetization vector can be easier visualized. Compared with the simulation in Figure 2.2f, a strong resemblance can be seen, an indication of the fact that the applied magnetic field pulse is indeed shorter than the precession frequency.

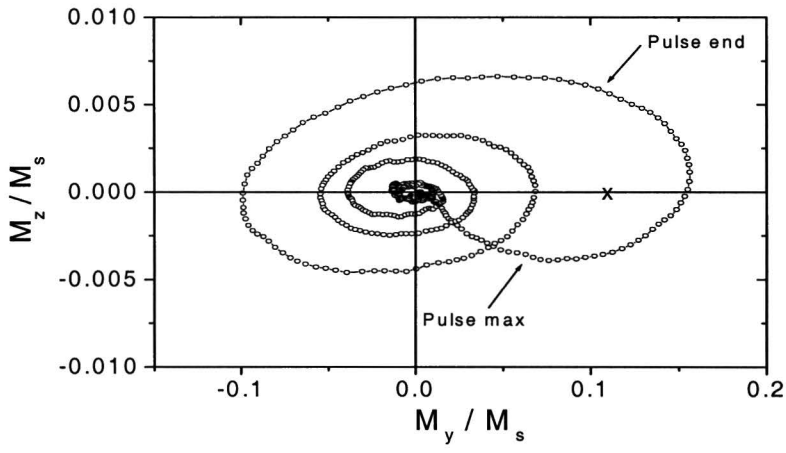

Figure 4.3: M_z-M_y-plot of the data of Figure 4.2 showing the excitation and the following damped precessional motion of the magnetization vector. The precession center, when the field pulse amplitude is maximal, is indicated with a cross.

A second measurement is carried out with the same bias field of 2.4 kA/m, but with field pulses of ~1.5 ns (see Figure 3.1b). The length of these pulses is much longer than the precession frequency, and precessional dynamics similar to the one shown in Figure 2.2c is expected.

The signals obtained from the two quadrants are shown in Figure 4.4. Applying the same phase correction procedure ($c_A = 0.87$, $c_B = 1.13$) and adding and subtracting the two signals yield after normalization the m_z and m_y time dependence as plotted in Figure 4.5. This picture shows strong similarities with Figure 2.2c, but contains also some interesting features that are not seen in the previous measurement and neither in Figure 2.2c.

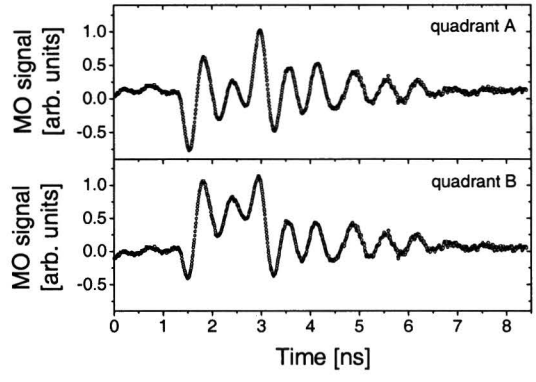

Figure 4.4: Raw lock-in data from two quadrants of the detector, normalized to the dc voltage on the detector. Pulse settings are Tr=5 and Tf=8, $t_{pulse} \cong 1.5$ ns, H_{bias}=2.4 kA/m along the x-axis.

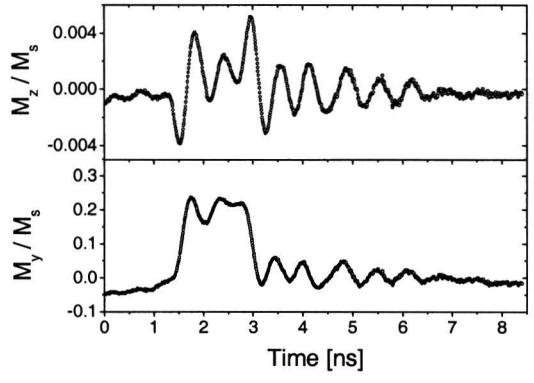

Figure 4.5: M_y and M_z calibrated to M_s, extracted from the raw lock-in data of Figure 4.4.

First, the m_y-data shows a negative value between 0 and 1 ns, a high positive value between 1.5 and 3 ns, and an oscillation around zero during the remaining 5.5 ns. The reason for this behavior can be seen in the voltage-pulse profile of Figure 3.1b. During the 1.5 ns before the rising edge of the voltage-pulse, the applied voltage is negative, which induces a current in the stripline that produces a field in the y-direction. Consequently, the effective field is not completely aligned in the x-direction and the magnetization acquires a component in the $-y$-direction. The duration of the pulse is about 1.5 ns and during this time the magnetization precesses around the effective field that now has a relative strong component in the $+y$-direction. After the field pulse is over, the voltage is essentially zero, so no current will be present and the magnetization precesses around the x-axis before damping out.

Second, the m_z-data shows an oscillation around m_z values that are slightly negative during the first 1.5 ns and positive between 1.5 and 3 ns. The LLG-model however, shows that this cannot be the case when the field pulse has no z-component, as shown in Figure 2.2c. This measurement data can be explained if the fact that the probe beam enters the HALO off-axis is taken into account. An off-axis entrance leads to a non-zero average angle of incidence and as a result, the probe beam is sensitive to m_x. Both quadrants will then pick up a signal with a component proportional to the change in m_x. The added signal will be not solely proportional to m_z, but to m_z *and* m_x, of course with different sensitivities (similar to quadrant A and B in Figure 3.11 and Table 3.1). So when the field pulse is at its maximum, the m_x-component will be significant and the added signal will show an oscillation of m_z around a non-zero value. The motion of the magnetization vector is even better illustrated when plotted in a m_y-m_z-t-graph as shown in Figure 4.6.

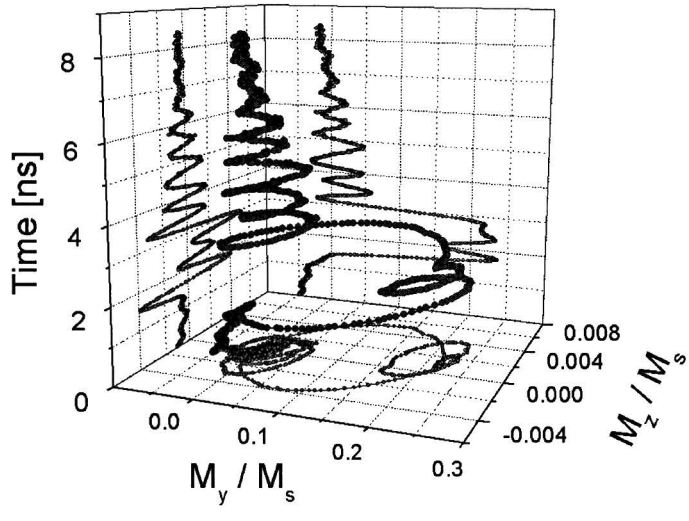

Figure 4.6: m_y-m_z-t-plot of the data of Figure 4.5, showing the excitation of the magnetization vector and the following damped precessional motion around two effective field directions. The first effective field is when the field pulse is present and the final effective field is the x-axis, when the field pulse has ended.

Sample B

In the optical setup used with sample B, the beam splitter is used since the absolute aperture of the microscope objective is too small to allow for an off-axis incidence of the probe beam. The Kerr-rotation proved to be larger for in-plane magnetization than the Kerr-ellipticty, so no λ/4-plate was inserted. This is not in contradiction with Figure 3.8, since the thickness of the Py layer (5 nm) is *less* than the typical penetration depth of light (13 nm), which means that equation (3.3) is not valid.

A typical measurement of the response of the magnetization vector to a magnetic field pulse of ~0.6 ns is shown in Figure 4.7. Here, the laser spot is focused at the center of the dot and no *external* magnetic field is applied. The static field is in this case the interlayer coupling field, which is directed along the x-axis. The calibrated M_z and M_y data from this measurement are shown in Figure 4.8. This figure is similar to Figure 4.2, as is expected since the same voltage pulse is applied. The ratio of the calculated sensitivities to m_z and m_y is found to be 140:1. As the variation in m_y was in this case also ~23 times larger than the variation in m_z, the m_z-signal is slightly more dominant in Figure 4.7 than in Figure 4.1, so the signals on quadrant A and B look very similar.

However, the m_y-data contains much more noise than the m_z-data. This may be due to a reduced Kerr-effect since the layer is thinner than the penetration depth of light. The precessional motion of the magnetization can be more clearly seen in Figure 4.9, which shows the m_z-m_y-plot of this measurement. From this figure we see that the magnetization is not uniformly spiraling towards the x-direction, as in Figure 4.3. This may be due to the specific shape of the magnetic field pulse. A long fall time of the pulse will cause a slow returning of the effective field to the x-direction, and relatively strong after pulsing can cause additional (small) excitations of the magnetization.

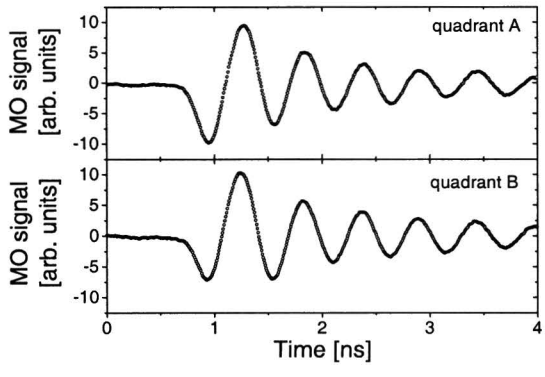

Figure 4.7: Raw lock-in data from two quadrants of the detector, normalized to the dc voltage on the detector. Pulse settings are Tr=2 and Tf=6, $t_{pulse} \cong 0.6$ ns, no bias field is applied.

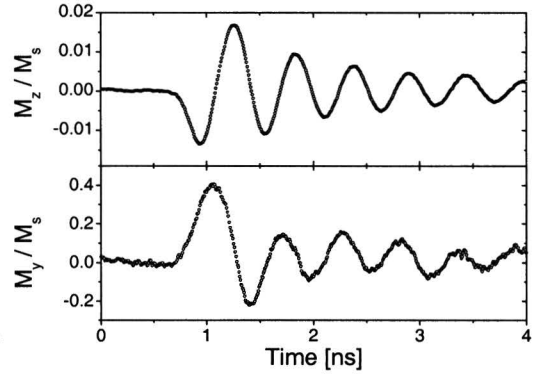

Figure 4.8: M_y and M_z calibrated to M_s, extracted from the raw lock-in data of Figure 4.7.

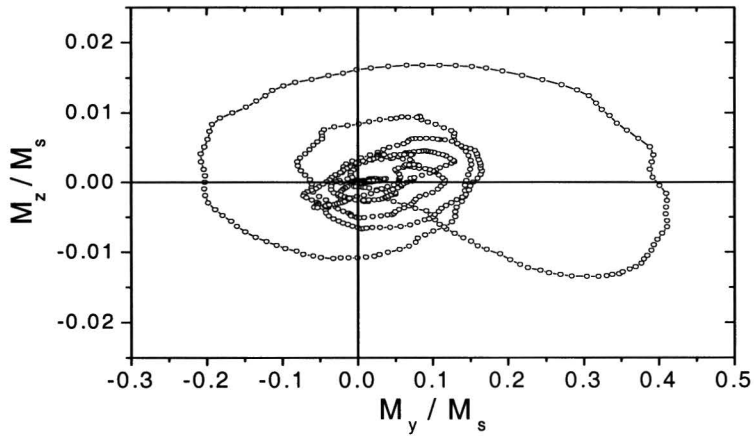

Figure 4.9: m_z-m_y-plot of the data of Figure 4.8, showing the excitation and the following the damped precessional motion of the magnetization vector.

In conclusion, we have shown that

- it is possible to extract the components of the magnetization vector from the signals of a four-quadrant detector.
- the signals obtained have a signal-to-noise ratio as high as 200:1.
- these two properties, combined with a spatial resolution of 1 μm and a temporal resolution well below 10 ps make this setup an excellent experimental tool to investigate the magnetization dynamics on small magnetic elements.
- the measured motion of the magnetization vector, induced by different magnetic field pulses, agrees well with the expectations from the numerical LLG-model.

4.2 Calculation of the field pulse profile

The measurements shown in the preceding section indicate that we observe a different response of the magnetization vector when voltage pulses with different shape are applied. For example, the 1.5 ns *voltage* pulse gives rise to magnetization dynamics expected from a ~1.5 ns *magnetic* field pulse. However, it is not clear to what extend the magnetic field pulse resembles the voltage pulses of Figure 3.1. In order to compare these two pulses profiles, equations (2.18) and (2.19) are used to calculate the magnetic field pulse profile from the measurement data. In these equations, derivatives and integrals of the measured data are required, which introduce some complications. In order to properly differentiate the measured data, some smoothing is required, since the differentiation operation is very sensitive to noise. As to the integration of the m_z-data, any offset in the signal must be removed, otherwise this will give a large linear contribution to the integrated data. Finally, the constants M_s, H_{bias}, α and γ_0 must be estimated in order to have the proper balance between the different terms. α can be extracted from the measurement data. Values for M_s and γ_0 for Permalloy dots have been obtained from

literature [11] but the strength of the bias field is less accurately known, due to calibration issues with our Gaussmeter. The calculated m_y and m_z can also contain some uncertainties, as a result of errors in the calibration procedure. In practice, the presence of oscillations, superposed to the pulse shape and with the same period as the measurement data, is a clear sign that the balance between the terms in equations (2.18) and (2.19) is not right. The dominant term can be found by looking at the phase of these oscillations.

Sample A

The measurement data of Figure 4.2 and Figure 4.5 are used to calculate the magnetic field pulse shapes. The results from these calculations are shown in Figure 4.10 and in Figure 4.11. Figure 4.10 shows that the calculation of the magnetic field pulse from both m_y-data and m_z-data yield the same profile, illustrating that the method gives unambiguous results. In Figure 4.11 only the calculation from the m_y-data is plotted, since the m_z-data could not be used due to a slight mixing with m_x, as mentioned earlier. The main features of the calculated field pulse agree well with the oscilloscope picture. After pulsing seen on the oscilloscope picture appears in the calculated field pulse as well. A major difference is the increased rise and fall time of the pulses, which is caused by contact imperfections and the impedance mismatch.

The amplitudes of both pulses depend on the calibration procedure, since an error in the procedure can e.g. lead a higher m_y value and consequently to a higher pulse amplitude, see equation (2.18). The amplitude of the 0.6 ns pulse is calculated to be 0.3 kA/m, slightly lower than the estimation of 0.4 kA/m with equation (3.1). This may be attributed to the impedance mismatch between the pulse generator and the sample waveguide, which causes amplitude losses at high frequencies. The amplitude of the 1.5 ns pulse, 0.45 kA/m, is higher than the 0.6 ns pulse, most likely because this pulse contains lower frequencies components that are not suppressed.

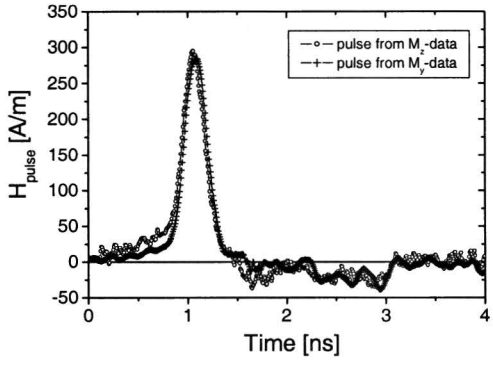

Figure 4.10: Magnetic field pulse calculated from both the m_y- and m_z-data of Figure 4.2, with the use of equation (2.18) and (2.19).

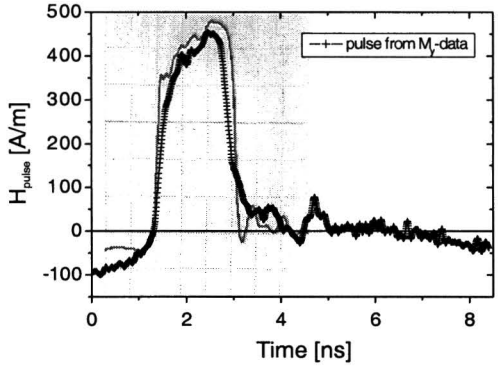

Figure 4.11: Magnetic field pulse calculated from the m_y-data of Figure 4.5, with the use of equation (2.18). The voltage pulse (Tr=5, Tf=8) is shown in the background.

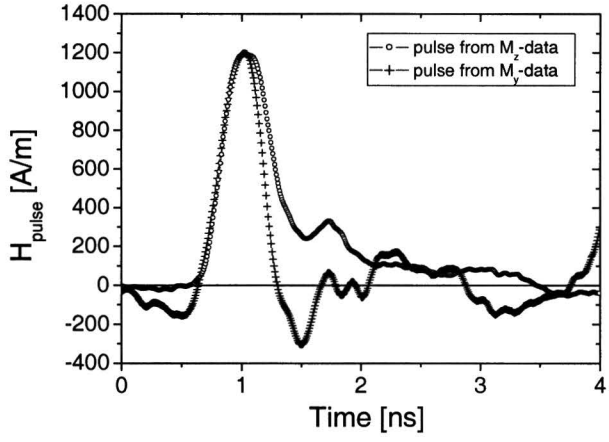

Figure 4.12: Magnetic field pulse calculated from both the m_y- and m_z-data of Figure 4.8, with the use of equation (2.18) and (2.19).

Sample B

The same procedure has been applied to the experimental data from sample B of Figure 4.8. The magnetic field pulses calculated from both the m_z and m_y data are shown in Figure 4.12.

In this case, the field pulses obtained with formulae (2.18) and (2.19) do not fully overlap. Although they both show a strong field pulse of approximately 0.7 ns, the pulse calculated from the m_z-data has a very long decay, whereas the pulse calculated from the m_y-data contains a sharp falling edge and strong after pulsing. The origin of these differences may lie in the fact that the approximation $M_x = M_s$, used in equations (2.18) and (2.19), is no longer valid in this case. During its precession, the magnetization vector makes an angle of 23.5° with the x-axis, which implies that at the extremes m_x has decreased by almost 10% (in the case of sample A this decrease was only 1%). Simulations with the numerical model show that the pulse, calculated from the m_y-data contains more after pulsing than the one calculated from the m_z-data. However, the differences in Figure 4.12 are much larger. Another reason for these differences may be that the 13 x 9 μm^2 element has a weak uniaxial in-plane anisotropy in the y-direction, as we will show in the next section, and this anisotropy is not included in the derivation of equations (2.18) and (2.19).

The pulse amplitude is results from the calibration procedure and therefore, the amplitudes of both pulses in Figure 4.12 are the same. The value of H_{pulse} = 1.2 kA/m is four times higher than the magnetic field pulse from sample A. The lower dc resistance and the reduced width of the current line are most likely responsible for this increase in amplitude. However, the amplitude of the field pulse is much lower than the estimated value of 2.1 kA/m with equation (3.1). We attribute this difference to the impedance mismatch at high (>3 GHz) frequencies.

In this section we have demonstrated the procedure to calculate the shape and amplitude of the magnetic field pulses. We can conclude that

- the method gives unambiguous results, since the calculation from both m_y-data and m_z-data give the same pulse shape, in the case of sample A.
- the obtained pulse shapes have a similar shape as the corresponding voltage-pulses.
- the method with formulas (2.18) and (2.19) may fail when more complicated magnetic structures are studied and larger excitations are induced.

4.3 Bias field dependence of the precessional motion

Sample A

A series of measurement have been performed on sample A to investigate the bias field dependence of the precessional motion. The measurement data was fitted with an exponentially damped sine-wave in order to extract the precession frequency and the characteristic time of the damped motion. The precession frequency as a function of the applied bias field is plotted in Figure 4.13. A fit to the Kittel-formula (first formula in (2.14)) is shown as well, with M_s = 900 kA/m .

The data agrees well with this formula down to 0.8 kA/m. At lower fields, a frequency could no longer be determined, due to two different reasons. First, the accuracy of the frequency obtained from the fit with an exponentially damped sine-wave became very low, since the oscillation period was comparable to the characteristic time of the damped motion. Second, the signal-to-noise ratio decreased due to less coherent motion of the spins across the laser spot at low fields. A typical example of this incoherent behavior can be seen in Figure 4.14, which shows a measurement with H_{bias} = 0 kA/m.

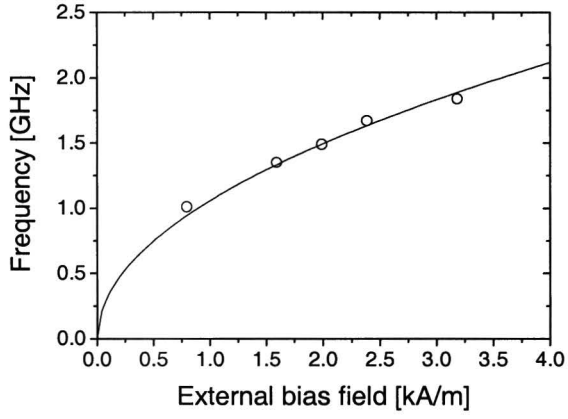

Figure 4.13: The precession frequency for different bias field strengths. A fit with the Kittel-formula (2.14) with M_s = 900 kA/m is also shown.

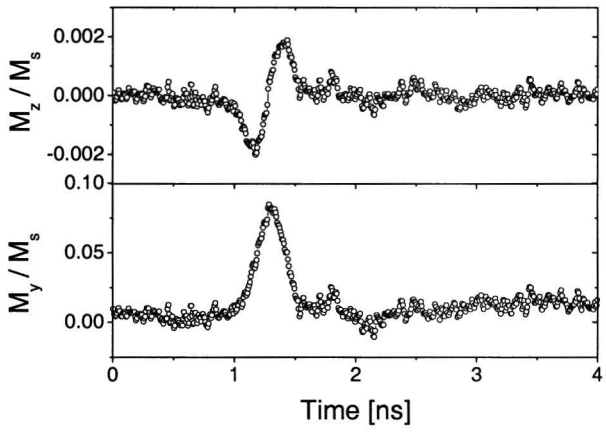

Figure 4.14: Response of the magnetization to a magnetic field pulse of 0.6 ns at zero bias field.

The spins show a coherent motion only in the presence of the magnetic field pulse. This means that the spins precess around different effective field directions due to local static fields (e.g. anisotropy) and only in the presence of the field pulse they have a common component in their motion.

The Gilbert damping parameter α, calculated from the characteristic time with equation (2.14), is equal to 0.011. It is indeed independent of H_{bias} down to 0.8 kA/m as expected when $H_x^0 \ll M_s$. This value for α is consistent with literature values for Permalloy [24].

Sample B

The precessional motion of the magnetization vector in the 13 x 9 μm^2 MTJ element has also been investigated as a function of the bias field. The frequency of the precession is determined from m_z-measurements that were fitted with an exponentially damped sine-wave. A 0.6 ns magnetic field pulse was used to induce the precessional motion. Two examples of m_z-responses are shown in Figure 4.15 as well as the fit parameters and the bias field.

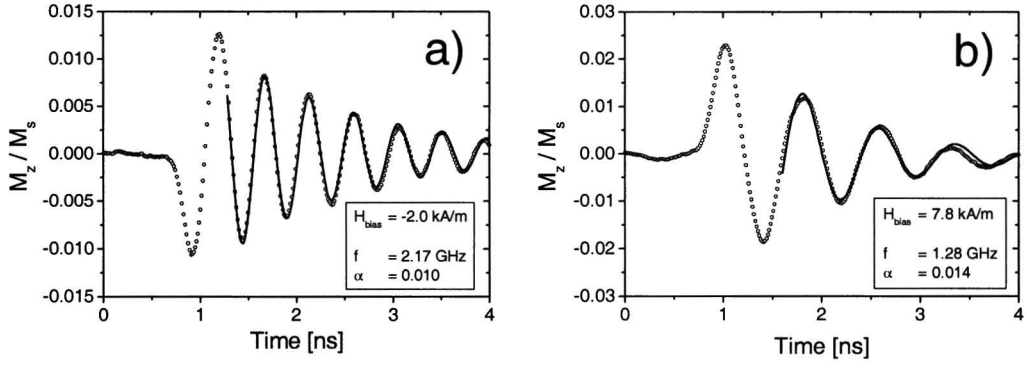

Figure 4.15: Response of m_z to a 0.6 ns field pulse with H_{bias} = -2.0 kA/m (a) and H_{bias} = 7.8 kA/m (b). The line is a fit with an exponentially damped sine-wave.

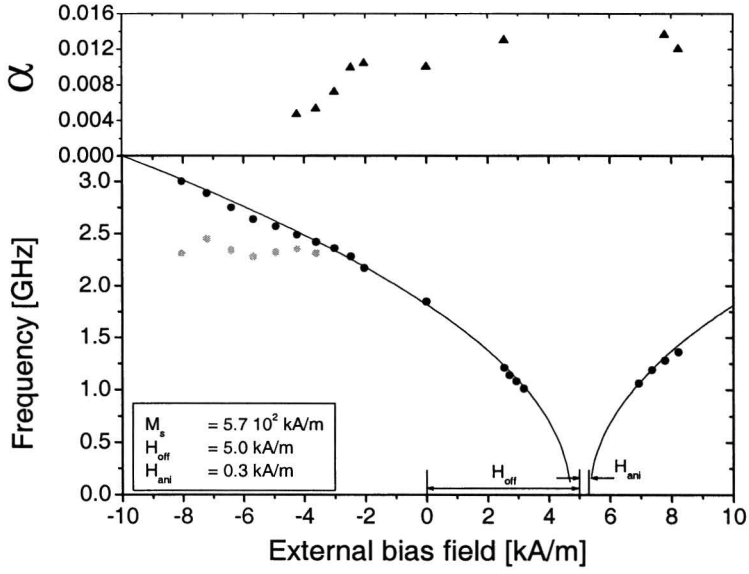

Figure 4.16: The precession frequency (black dots) and damping parameter α (black triangles) as a function of the applied bias field in sample B. A fit to a modified Kittel-formula is shown, as well as the parameters of the fit. The gray dots indicate the second frequencies, obtained from a fit with two exponentially damped sine-waves.

The sign of the m_z-excitation is different in the two measurements, as a result of a different direction of the torque. As the magnetization of the Py-layer is opposite in the two cases due to the bias field, the direction of the torque is opposite as well. The calculated frequencies from the whole measurement series are plotted in Figure 4.16 as a function of the applied bias field in the x-direction. In Figure 4.16 the values of the Gilbert damping parameter α are also indicated, for those m_z-responses from which it could be deduced. Due to the coercivity of the magnet, it was not possible to perform measurements at fields below the coercive field.

In order to fit the main frequency data (black dots) in Figure 4.16, modification of the Kittel-formula in (2.14) was necessary. The interlayer coupling field introduces an offset in the bias field, H_{off}, at which the frequency drops to zero. However, it turned out that two different offset fields were required in order to fit both the data at fields smaller and larger than 5 kA/m, if symmetry between the left and right curve is assumed. A gap of magnitude 0.6 kA/m arises between the two fields at which the frequency drops to zero. This behavior can be attributed to a uniaxial anisotropy in the y-direction, which can be accounted for by including an anisotropy term in the Kittel-formula, which now takes the form

$$\omega = \gamma_0 \sqrt{\left(-H_{ani} + \left|H_{bias} - H_{off}\right|\right)\left(\left(M_s - H_{ani} + \left|H_{bias} - H_{off}\right|\right)\right)}. \qquad (4.1)$$

The fit to the experimental data as well as the fit parameters are shown in Figure 4.16. The low value of M_s originates from the low thickness of the Py-layer. As the thickness of a magnetic layer drops below 10 nm, the saturation magnetization is known to decrease

as surface effects become more and more important, see [18]. The value for the interlayer coupling field, 5.0 kA/m, is in agreement with the SQUID measurement of Figure 3.6. The anisotropy field cannot be accounted for by considering only the shape anisotropy of this element. The approximate formula for the demagnetization factors in a rectangular element is $N_i \approx 2t/\pi l_i$, with t the thickness of the layer and l_i the length of the element in the direction i [25]. For the 13 x 9 μm^2 element, this formula gives $N_x = 0.00035$ and $N_y = 0.00025$. These factors result in an anisotropy field of only 0.06 kA/m, much lower than the anisotropy field calculated from the fit (0.3 kA/m).

Another indication for a relative high anisotropy in the y-direction comes from a measurement of the initial excitation of m_z as function of the bias field. This measurement was performed at a fixed position (center of the element) and at a fixed time delay (50 ps after the field pulse). The result is shown in Figure 4.17. We see that the amplitude of m_z changes sign in the region where 4.4 kA/m < H_{bias} < 6.4 kA/m, as a result of the reversal of the magnetization direction of the NiFe-layer. The amplitude is zero at $H_{bias} = 5.2$ kA/m, indicating that the magnetization direction is rotated towards the pulse field direction. The width of the switching region can thus be attributed to an anisotropy field in the y-direction. This bias field value is comparable to H_{off} determined from Figure 4.16. The relatively high anisotropy that shows up in Figure 4.16 and Figure 4.17 is probably growth related. The crystalline anisotropy in the element can be obtained from the hysteresis loop in Figure 3.6b, which gives 0.5 kA/m. This crystalline anisotropy may have its easy axis in the y-direction due to the small shape anisotropy.

The Gilbert damping parameter α is also plotted in Figure 4.16 as a function of the external bias field. In the region with bias fields between –2.5 and 1 kA/m, the damping parameter is about 0.01, in agreement with values found in literature [24]. At high positive bias fields, the damping parameter increases, probably due to the fact that the spins are moving less coherently, which allows them to lose their spin momentum more easily.

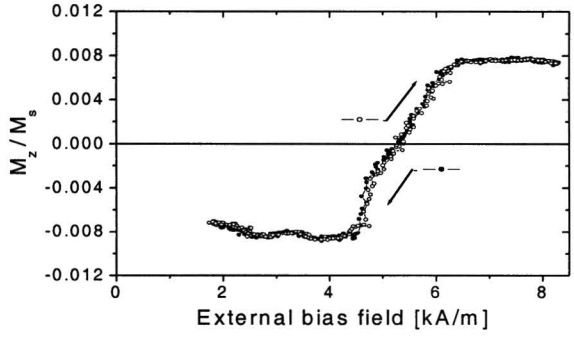

Figure 4.17: Excitation of m_z as function of the bias field at fixed position (center of the element) and fixed time delay (50 ps after the onset of the pulse). The two directions of the field sweep are indicated.

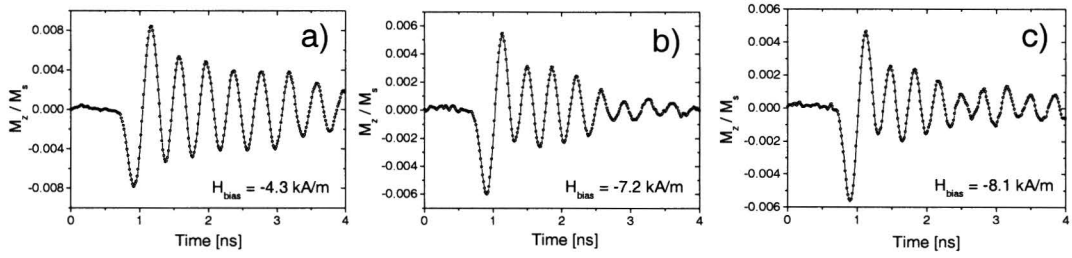

Figure 4.18: Response of m_z to a 0.6 ns field pulse with a bias field of –4.3 kA/m (a), –7.2 kA/m (b) and –8.05 kA/m (c).

At large negative fields, the damping parameter decreases, which is quite surprising. Moreover, at fields below –4.5 kA/m, a damping parameter could not be extracted from the fit, as the amplitude of the M_z-oscillation was not exponentially decreasing. We see at the same time that this frequency deviates from the Kittel-fit. Three examples of M_z-measurements that illustrate these findings are shown in Figure 4.18.

Figure 4.18a clearly shows a reduced damping. However, Figure 4.18b suggests the presence of a second frequency, which shows up as an envelope structure around the oscillation, indicating a beating effect. The small damping observed in Figure 4.18a may thus be an apparent damping due to this second frequency. Figure 4.18c also shows a kind of envelope structure. These measurements at large negative field have been fitted with two damped sine waves, in order to extract the possible second frequency. One frequency was fixed at a value corresponding to the Kittel-fit, with fixed damping parameter. The second frequencies obtained this way are shown as gray dots in Figure 4.16, and are more or less constant as a function of field (~2.3 GHz). This second frequency could be a sign of a different spin mode, coexisting with the uniform precession. However, the origin of this second spin mode in the central region of the element at high bias fields is not yet understood.

In the analysis of the data, possible effects due to the magnetic field pulse have to be included. Especially at high frequencies, the motion of the magnetization becomes more sensitive to the precise shape of the field pulse. For example the orientation of the magnetization vector at the moment the field pulse ends will determine the amplitude of the following oscillations. After pulsing will also have a stronger influence on the precessional motion. In order to account for these effects of the field pulse, its precise shape must be determined.

In this section we have studied the frequency dependence of the precession as function of the applied external magnetic field. The main conclusions are:

- The precession frequency dependence in sample A is in agreement with the Kittel-formula down to 0.8 kA/m.
- No frequency could be determined at lower fields, due to less coherent behavior of the spins.

- The frequency dependence in sample B can be fitted with a Kittel-formula, modified with the contribution from a uniaxial anisotropy in the *y*-direction.
- The observed anisotropy in the y-direction is attributed to crystalline anisotropy, as it cannot be explained solely by shape anisotropy.
- At large negative fields the observed frequencies deviate from the Kittel-fit. A second frequency from a different spin mode appears to be present, however, a complete understanding of the origin of this second spin mode needs more research.
- The Gilbert damping parameter α changes as a function of applied bias field. At bias field > 2 kA/m, the origin of a higher damping may be a less coherent behavior of the spins. At bias field < −2.5 kA/m, it can be an apparent damping due to the possible presence of a second spin mode.

4.4 Large angle excitations

In the regime with bias field values between 3.3 and 6.7 kA/m, it was not possible to fit the data with an exponentially damped sine-wave. In this region, the difference between the bias field and the interlayer coupling field is below 1.5 kA/m. Consequently, the spins are less pinned in the *x*-direction. The magnetic field pulse, with amplitude of 1.2 kA/m, is then comparable or even larger than the static field in the element. At bias fields close to the interlayer coupling field, the uniaxial anisotropy in the *y*-direction also becomes important. The anisotropy *field* (in the *x*-direction) can rotate the equilibrium direction of the magnetization towards the *y*-axis and can change the response of the magnetization to a field pulse. It will be no surprise that the motion of the magnetization vector in these cases will not be a simple precession around an equilibrium direction.

We will consider three examples of this motion, measured at bias fields 3.7, 4.3 and 6.6 kA/m, in order to show the main features we have observed. The first example (H_{bias} = 3.7 kA/m) is shown in Figure 4.19.

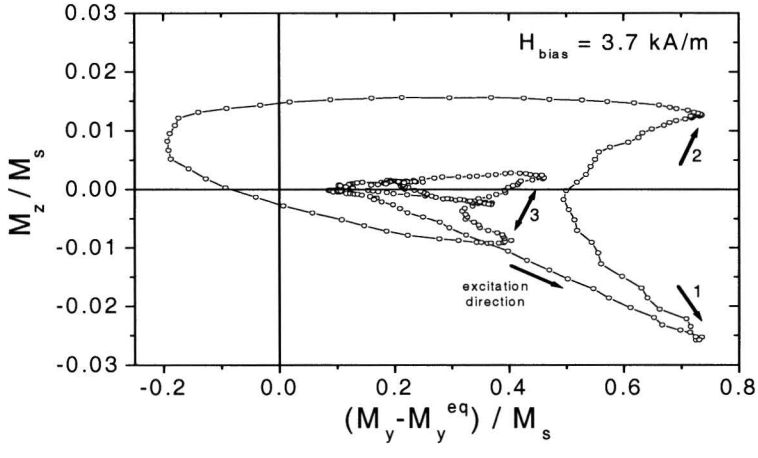

Figure 4.19: m_z-m_y-plot of the magnetization response to a 0.6 ns field pulse at a bias field of 3.7 kA/m.

This m_z-m_y-plot clearly shows the excitation of the magnetization vector, with both m_y and m_z departing from zero. At first sight, it looks as if the magnetization vector turns at the moment when $m_y \cong 0.75$, instead of making an elliptical trajectory. A second turn (arrow 2) occurs again at $m_y \cong 0.75$. This behavior can be explained if we remember that the m_z-m_y-plot is a projection of the tip of the magnetization vector on the m_z-m_y-*plane*. Points with the same m_y and m_z but opposite m_x show up on the same position. In the case of Figure 4.19a, we see the magnetization vector rotating to negative m_x-values and back towards the equilibrium direction. At arrows 1 and 2, the direction of the magnetization is aligned along the y-axis. The fact that at these points the measurement gives $m_y \cong 0.75$, instead of $m_y = 1$, can be attributed to a rotation of the equilibrium direction towards the y-axis. This is also the reason that the horizontal scale is denoted as the difference in M_y from the equilibrium value. The equilibrium value in Figure 4.19 is $m_y \cong 0.25$, corresponding to an angle of 14° with the x-axis. We attribute the rotation of the equilibrium axis to the uniaxial anisotropy in the y-direction. The above statement is of course only justified when the length of the magnetization vector is unity, thus with full coherence between the spins, which we expect is the case during the presence of the field pulse.

At arrow 3 we see again a signature that the magnetization vector rotates to negative M_x-values. However, the signal is much less, which may be an indication of a loss of coherence between the spins. If not all the spins participate in a coherent motion, some random motion from these non-participating spins will be present. This random motion will average to zero, so the average (and measured) direction of the magnetization will still be the one of the coherent motion. The magnitude of the magnetization vector, however, will in this case be less than unity and show up in the measurement as a reduced signal.

It can also be seen that at the start of this measurement, the magnetization direction makes an angle of 20° ($m_y = 0.35$) with the x-axis, instead of 14°. This means that the direction of the magnetization between the situation with a current pulse train and without a current pulse train is different. The time between two successive magnetic field pulses (12.2 ns) is not long enough to reach the equilibrium state of the situation without current pulses. A current pulse train thus seems to give rise to a net magnetic field in the y-direction, which is the origin of the changed equilibrium direction.

The fact that the magnetization rotates to negative m_x, showing up as the turning points at arrows 1 and 2, provides a way to correct for any crosstalk between the signals for m_y and m_z, as the m_y values at arrows 1 and 2 must be the same. The correction factors of the two quadrants for the measurements discussed in this section are only ~0.95 and ~1.05. These correction factors are constant within 0.01 for the whole measurement series and thus only depend only on the alignment of the optical setup, as was the case with sample A. The condition of full coherence between the spins must of course be met.

At a slightly higher bias field, H_{bias} = 4.3 kA/m, a different large angle excitation is observed as shown in Figure 4.20a. In this case, the initial and final direction of the magnetization after 4 ns are not the same. After the field pulse ends, the magnetization rotates towards m_y = 0.96, which indicates a switch of ϕ_s = 45°. If we take into account that the length magnetization vector decreases after the field pulse ends, the real switch direction may in fact be closer to the *y*-axis, thus along the anisotropy direction. During the last 1.5 ns of the measurement, the magnetization already starts to relax towards the equilibrium direction. Of course, during the remaining 9 ns before the next magnetic field pulse arrives, the magnetization has relaxed back to the equilibrium direction, otherwise no stroboscopic measurement would have been possible. The motion of the magnetization vector can be visualized in three dimensions if when we consider the length oft the magnetization vector constant. The result is shown in Figure 4.20b. The angle of the magnetization with the *x*-axis at the start of the measurement, ϕ_i = 29°, is indicated, as well as the excitation angle ϕ_e = 119°.

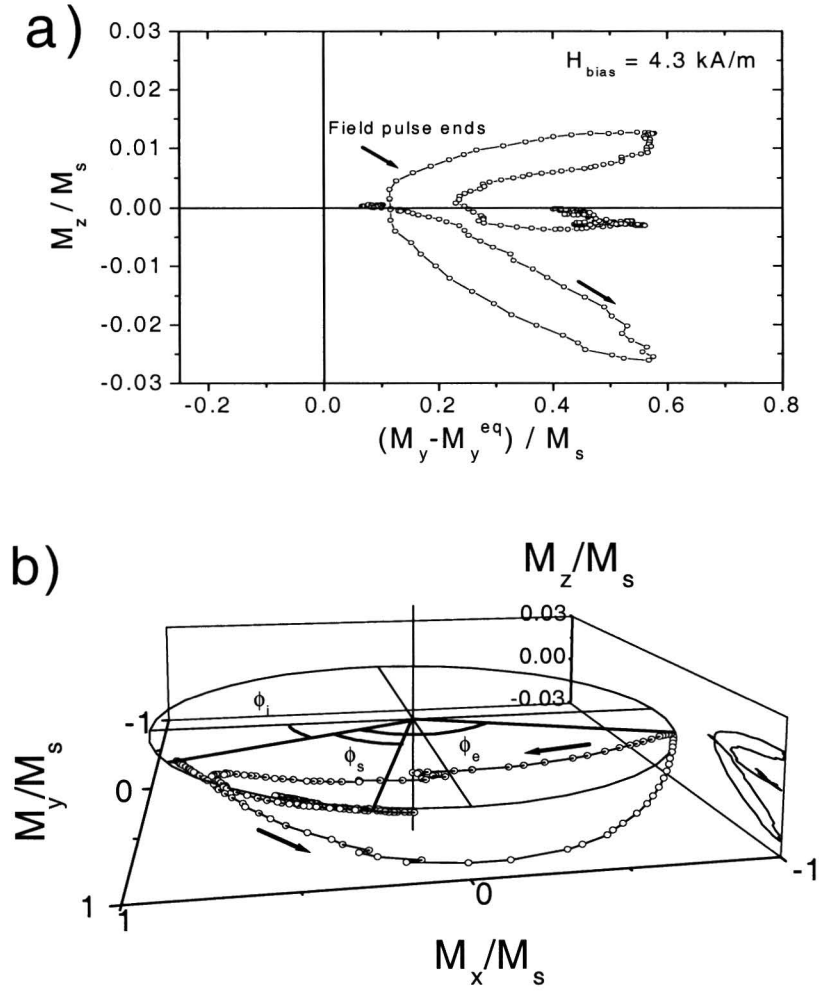

Figure 4.20: (a) m_z-m_y-plot of the magnetization response to a 0.6 ns field pulse at a bias field of 4.3 kA/m. (b) The motion of the magnetization vector visualized in three dimensions. The projection of this motion on the y-z-plane is also shown.

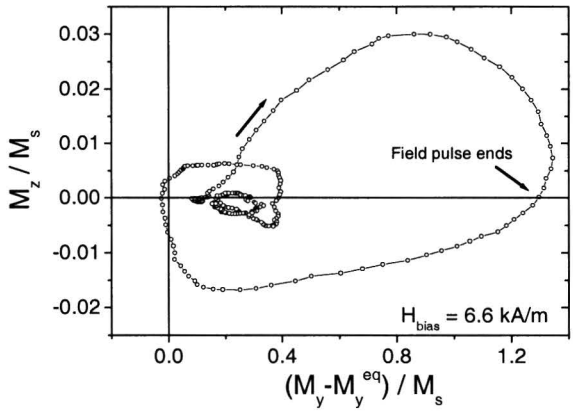

Figure 4.21: m_z-m_y-plot of the magnetization response to a 0.6 ns field pulse at a bias field of 6.6 kA/m.

As a final example, we consider a measurement taken with a bias field of 6.6 kA/m. In this case, the bias field is larger than the interlayer coupling field, so the equilibrium direction of the magnetization will have a component in the *–x-direction*, instead of the *+x-direction*. The direction of the torque is therefore opposite as well as the excitation of the magnetization vector. Figure 4.21 shows the m_z-m_y-plot of the measurement and the reversed direction of the magnetization excitation. Since the interlayer coupling is over-compensated by only 1.5 kA/m, a large angle motion is observed. There is, however, no sign of rotating of the magnetization towards *positive* m_x. Instead, calibrated M_y values are observed that exceed unity, an indication that the equilibrium axis has rotated towards the *negative* y-axis. From the maximum of the measured M_y-signal (M_y / M_s = 1.34), we conclude that the equilibrium direction makes an angle of 20° with the negative x-axis in this case.

In summary, the examples shown in this section indicate that

- large angle excitations of more than 120° can occur is the 13 x 9 μm^2 element at bias field comparable to the interlayer coupling field.
- during these excitations the magnetization vector rotates towards negative x-values.
- the magnetization can switch towards the y-axis and that it slowly relaxes to the equilibrium direction.
- signs of decoherence between the spins are observed.
- the equilibrium direction rotates towards the y-axis, as a result of a uniaxial anisotropy in the y-direction.
- due to this anisotropy in the y-direction no 180° switch events can occur in this element.

4.5 Spatially resolved measurements

So far, the measurements shown and discussed were performed on the center of the ferromagnetic elements. In this section, we will present spatially resolved measurements of the magnetization dynamics in the 13 x 9 μm^2 element of sample B.

Line scans

We will start with measurements of the response of the magnetization to 0.6 ns magnetic field pulses at several positions along different lines on the sample, shown in Figure 4.22.

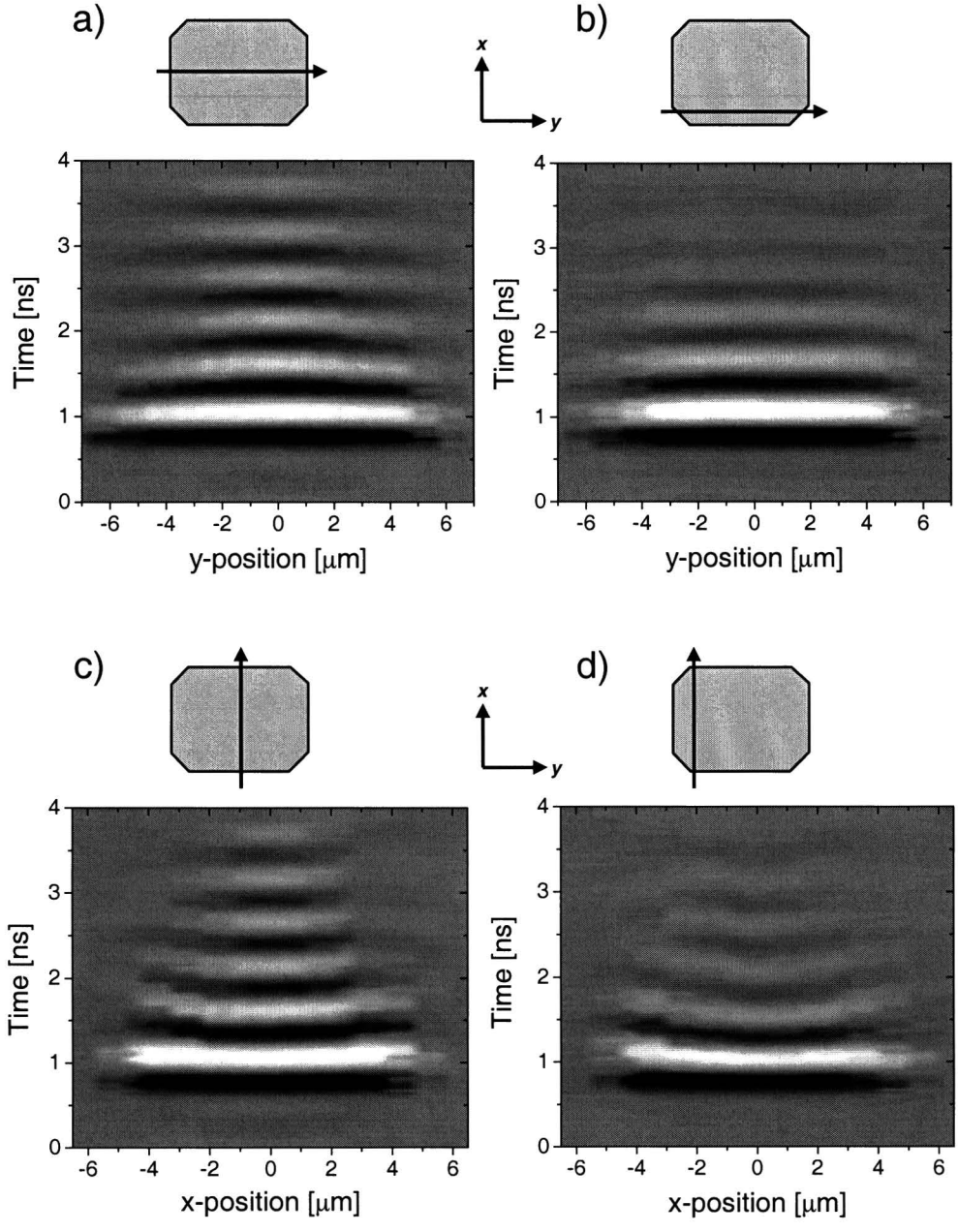

Figure 4.22: Time response of m_z as function of position along several different lines along the sample. (a) and (b) are scans in the y-direction, (c) and (d) are scans in the x-direction.

No external bias field is applied in these measurements. Before each time scan, the sample is moved by 0.5 μm with the translation stage. It must be noted that the translation stage can be moved with a limited accuracy of 1 μm, which may cause errors in determining the exact position of the laser spot. In these measurements, only the M_z-component is measured.

The central scan in the y-direction shows that the center of the dot (y=0 in Figure 4.22a) the precessional motion is the same as the one shown in Figure 4.8. However, when moving to the edge of the sample (to $y = -5$ or $y = 5$), the amplitude of the precessional motion after the first oscillations becomes much smaller. Furthermore, the 'waves' seem to be curved a bit, indicating a higher precession frequency at the edge compared to the center of the sample. The edge-scan in the y-direction (Figure 4.22b), shows a more uniform response of the magnetization as a function of position, as well as a higher damping of the precessional motion.

These effects are even more pronounced in the time response measurements at different positions along lines in the x-direction. The higher damping at the edges ($x \cong -4$ and $x \cong 4$ in Figure 4.22c) can be clearly seen. The curvature of the 'waves' is now upward and more pronounced, indicating a lower frequency at the edges compared to the center. This curvature and higher damping of the precession also show up in the edge-scan of Figure 4.22d.

We attribute the origin of this behavior to the internal effective field in the element, which is highly inhomogeneous. This inhomogenity is caused by the demagnetization fields at all four edges, and the stray field from the lower CoFe-layer at the edges parallel to the direction of the magnetization of the CoFe-layer, as explained in section 2.5. The edges parallel to the x-axis correspond to edge 1 in Figure 2.7, where the precession frequency is higher. The edges parallel to the y-axis correspond to edge 2 (lower frequency). In addition to the missing dipole field at edge 2, it is also the stray field from the CoFe layer that is in competition with the interlayer coupling field. Therefore, at these edges the change in frequency will be larger than at the edges parallel to the x-axis.

For Figure 4.22c, the precessional motion after the field pulse is fitted with an exponentially damped sine-wave in order to extract the frequency and the damping parameter as function of position. The result is shown in Figure 4.23.

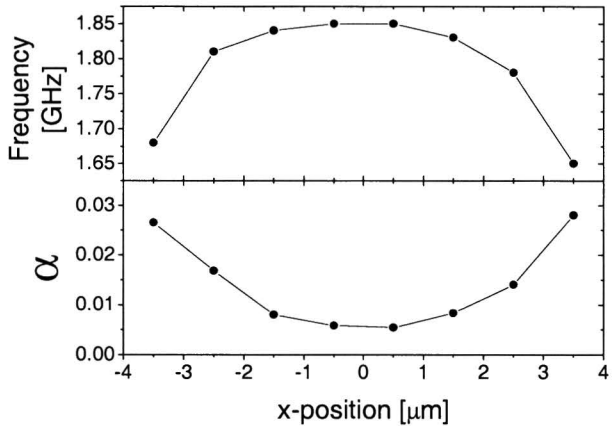

Figure 4.23: Frequency and damping parameter α as function of position for the line scan of Figure 4.22c.

The figure explicitly shows a lower frequency of 1.68 GHz near the edge compared with the central frequency of 1.85 GHz. This frequency difference corresponds to an effective field difference of 0.8 kA/m, which is an indication of the strength of the strayfield. At the same time the damping parameter α is increasing from 0.006 in the center to 0.028 near the edge. The origin of the increased damping of the precession near the edges can be attributed to an inhomogeneous behavior of the edge spins. Another mechanism can be an efficient energy transfer from the edge mode to the uniform spin mode.

Full time resolved surface scan

In order to get a spatially resolved image of the magnetization response of the *full* element, raster scans have been made with different positions of the delay line, i.e. at fixed time delay between the laser pulse and the magnetic pulse. During each raster scan, both M_z and M_y have been measured. The measurement was performed in the absence of an external bias field and with a magnetic field pulse of ~0.6 ns. After each raster scan, the time delay was increased by 50 ps. The individual frames, showing the spatially resolved M_z-component of the magnetization, are plotted in Figure 4.24.

From this figure we see that there is a uniform excitation of the magnetization over the whole element (frame 2-6). However, after just 300 ps a deviation from this uniform motion can be seen (frame 7). This behavior is even more pronounced in frames taken at longer delay times, e.g. frames 15 and 20. We see that the precession of the magnetization at the left and right edges is advanced in time compared with the center. In the same time, the precession of the magnetization at the top and bottom edges lags behind, compared with the center of the element. Figure 4.24 thus shows exactly the behavior that is observed in Figure 4.22.

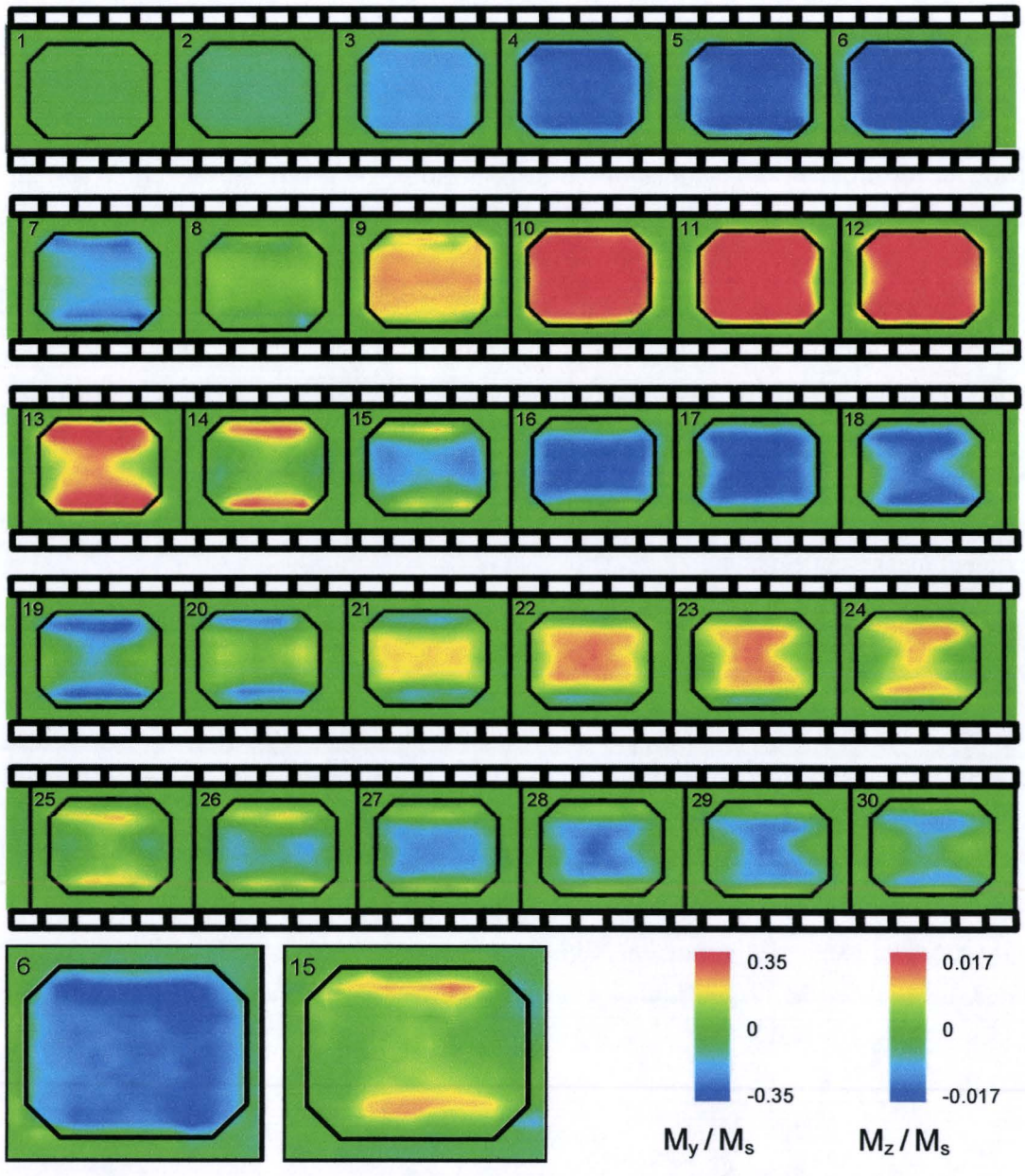

Figure 4.24: Full surface scans of the m_z response to a 0.6 ns magnetic field pulse with $H_{bias} = 0$ kA/m (top frames 1 – 30). The time step is 50 ps, the field pulse start at frame 1. The my response is shown as well for two different time (bottom left frames 6 and 15). The color scales for m_y and m_z are also shown.

In addition, two frames that show the in-plane magnetization are also included. Frame 6 shows a quite uniform excitation in the *y*-direction due to the field pulse. A spatial non-uniform m_y can be seen in frame 15. If we compare this picture with the frame 15 of the m_z data, we see that where m_z is large, m_y is low and vice-versa, as should be the case with precessional motion.

Bias field dependence of m_z

The claim that the stray field from the lower CoFe-layer is responsible for a change of the internal effective field at the edges perpendicular to the x-axis, implies the effect will be different for different orientations of the magnetization in the NiFe-layer. In the case of parallel directions of the magnetization in the two ferromagnetic layers, the stray field will be directed opposite to the magnetization of the NiFe-layer and thus give rise to a lower internal effective field. However, when the directions of the magnetizations are anti-parallel, the stray field will be in the same direction as the magnetization of the NiFe-layer and result in a higher internal effective field. This implication can be experimentally verified by using an external bias field to change the direction of the magnetization in the NiFe-layer. Figure 4.25 shows two raster scan measurements of the m_z-component of the magnetization at a fixed time delay (100 ps after the onset of the pulse) with two different external magnetic fields.

In Figure 4.25a the bias field is 4 kA/m, which is lower than the interlayer coupling field (5.1 kA/m). The equilibrium magnetization direction in the NiFe-layer is thus directed along the $+x$-axis. We see a reduced amplitude of the M_z-component at the top and bottom edge, indicating a slower response to the field pulse. The internal effective field will thus be lower at these edges, in agreement with our expectations. When the bias field is larger than the interlayer coupling field, as in Figure 4.25b with H_{bias} = 7 kA/m, the magnetization in the NiFe-layer will be directed along the $-x$-axis. In this case, we do not see a strong reduction of the amplitude of the M_z-component near the edges. As the magnetization of the NiFe-layer is reversed, the stray field will be in the same direction as the magnetization and will oppose the demagnetization field near the edges.

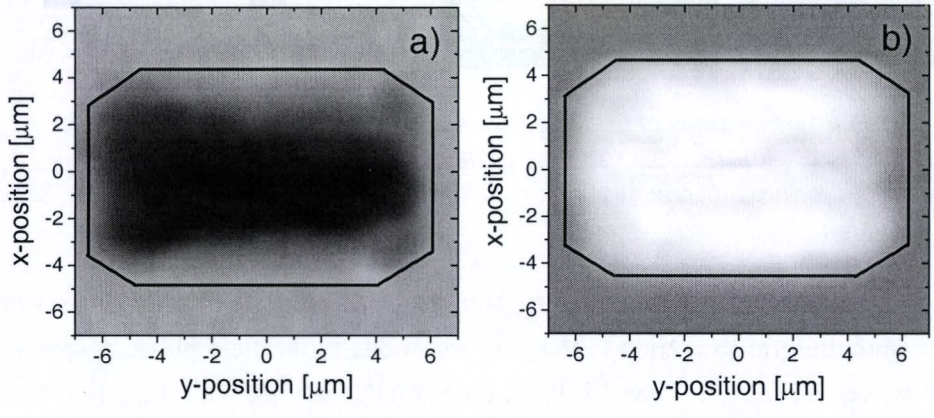

Figure 4.25: Surface scan of the element showing the m_z-component of the magnetization 100 ps after the onset of the field pulse. H_{bias} = 4 kA/m in (a) and H_{bias} = 7 kA/m in (b).

Domain imaging

Another application of these raster scans is using the response of the magnetization to a magnetic field pulse at zero internal field to obtain information about the static domain structure in the element. When the interlayer coupling field is fully compensated by an external bias field, a domain pattern will form in the element due to the presence of a uniaxial anisotropy, the demagnetization fields and the stray fields at the edges. The response of the magnetization to a field pulse will depend on the initial local orientation of the magnetization in the element. For example, when the magnetization is parallel to the pulse field, no excitation will occur, since the torque is zero. When the magnetization is perpendicular to the pulse field, the sign of the M_z-signal will reveal whether the magnetization was aligned parallel or anti-parallel to the x-axis.

Figure 4.26 shows a raster scan of the element at a time delay fixed to about 50 ps after the onset of the field pulse, with a bias field of 5.2 kA/m, which almost compensates the interlayer coupling field (see Figure 4.17). A clear domain structure can be seen in this raster scan. The black (white) regions indicate a magnetization with a strong component in the $+x$-direction ($-x$-direction), as the response in the M_z-component is downward (upward). In gray areas, the magnetization is aligned more or less along the y-axis. With this information we can reconstruct the domain pattern in the unbiased (interlayer coupling fully compensated) element, which is schematically drawn in Figure 4.26b. From this we see the influence of the strayfield at the horizontal edges. It aligns the spins perpendicular to the edge. In the center, the spins are aligned in the y-direction due to the anisotropy in that direction.

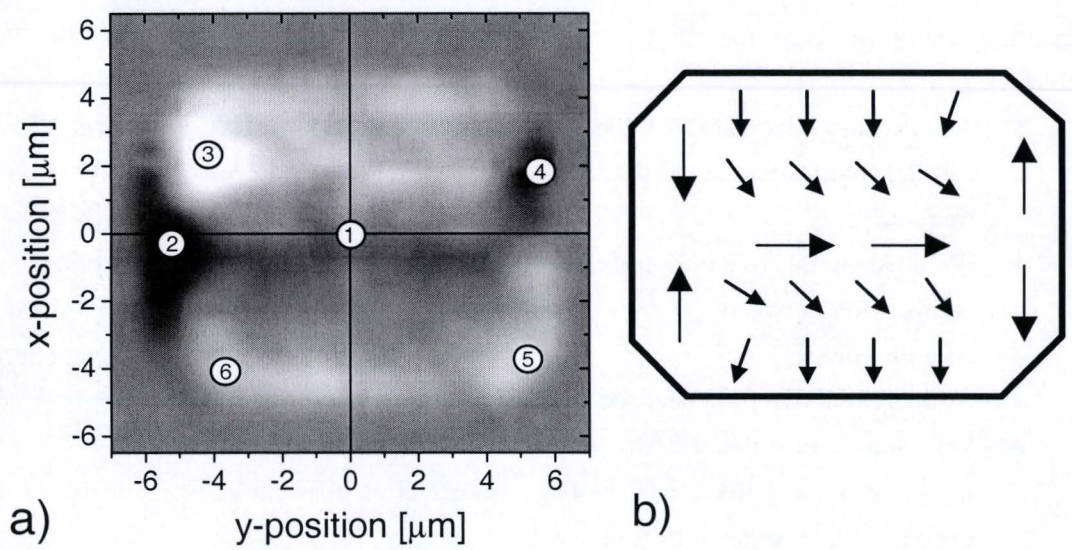

Figure 4.26: (a) The response of the magnetization to a 0.6 ns magnetic field pulse. White (black) areas indicate spins moving upward (downward) with respect to the plane of the element. The bias field is 5.2 kA/m, almost compensating for the interlayer coupling field. (b) A schematic drawing of the domain pattern that can be deduced from the data in (a).

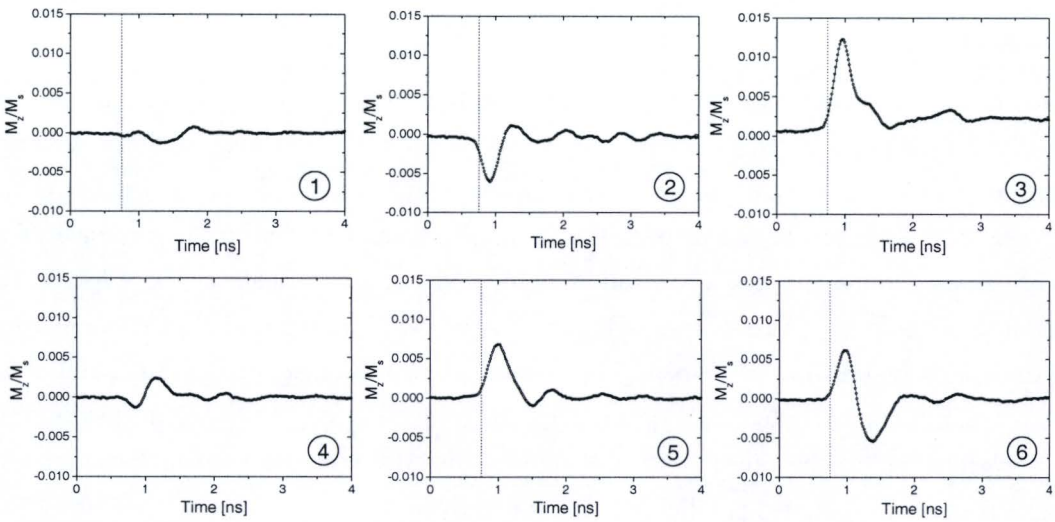

Figure 4.27: Full time response measurement of m_z to a 0.6 ns field pulse with H_{bias} = 5.2 kA/m. The numbers correspond to the position indicated in Figure 4.26.

To demonstrate that the response of the magnetization is indeed very different on different positions on the unbiased sample, the full time response is measured at the six different positions indicated in Figure 4.26. The responses are shown in Figure 4.27. In the center of the dot, position 1, almost no response of the magnetization is visible. This is a clear sign that the magnetization was aligned along the pulse field direction. At the other five positions, we see different excitations that depend strongly on the local effective field direction as well as the strength. The correspondence between the excitation direction and the gray-scale in Figure 4.26 is unambiguous.

From spatially resolved measurements shown in this section, we can conclude the following:

- An increase (decrease) of the precession frequency is observed at the edges parallel (perpendicular) to the interlayer coupling field, compared with the center frequency.
- We attribute this to a non-uniform effective magnetic field in the element due to a competition between the demagnetization field and strayfield with the interlayer coupling field.
- An increased damping near the edges is observed.
- We have postulated two mechanisms for this behavior, namely an inhomogeneous behavior of the edge spins and an efficient energy transfer from the edge mode to the uniform mode.
- The complete vector resolved time response of the element to a magnetic field pulse can be imaged with a spatial resolution of ~ 1 μm.
- It is possible to image the domain structure of an element by measuring the initial m_z-response to the magnetic field pulse.

5 Conclusions and outlook

In this Thesis we have studied magnetization dynamics in the precessional regime in microscopic magnetic elements. A measurement technique has been developed to detect all components of the magnetization vector simultaneously with high spatial and temporal resolution. This measurement technique is based on a four-quadrant detection scheme. We have shown its ability to detect two of the three components of the magnetization vector with a signal-to-noise ratio as high as 200:1. With an electrical pump / optical probe setup and a high aperture microscope objective, a temporal resolution beyond 10 ps and a spatial resolution of ~ 1 μm is achieved, which allows investigation of the local magnetization dynamics in micromagnetic elements. This technique is less complicated than e.g. second harmonic generation and is at least as sensitive as other currently used vectorial measurement schemes.

Although a lot of emphasis was on the validation of this vectorial measurement technique, we have also observed interesting physics in exchanged biased magnetic tunnel junctions that deserves further investigation. In summary,

- We have observed signs of a second spin mode in the center of the MTJ-element that appears at high bias fields. The precise origin of this mode, its dependence on the bias field and a possible relationship with edge modes still needs to be determined.
- Raster scans of the element show the presence of local spin modes, which results from a competition between the demagnetization field, strayfield and the interlayer coupling field present in the element. The dynamics thus strongly depends on the local effective field.
- An increased damping of the precessional motion is observed at the edges of the element. Two possible mechanisms for the enhanced damping were mentioned, however, the *precise* mechanism responsible has yet to be established.

- The dynamical response of the magnetization to a magnetic field pulse can be used to image the static domain pattern in the element, as the interlayer coupling field is fully compensated by an external effective field.
- We have measured large angle excitations of the magnetization vector, but no full 180° switching.

Suggestions for improvements of the setup presented in this work and recommendations for further research are the following:

- To push the spatial resolution of the setup beyond 1 μm, a microscope objective with a higher numerical aperture can be used. Alternatively, reducing the wavelength of the laser light will also improve the spatial resolution and can be easily implemented, as a frequency doubler is available.
- In order to more accurately control of the position of the sample, piezo actuators can be used.
- Two pairs of Helmholtz coils that can produce uniform fields in both in-plane directions higher than 15 kA/m will allow for setting an in-plane field in any direction and increase the bias field window in which the magnetization dynamics can be studied.
- The *precise* shape of the magnetic field pulse, induced in the MTJ-elements, needs to be determined in order to correct for possible after pulsing and to allow realistic simulations with the numerical LLG-model. Extension of the formulae for the pulse calculation is necessary, in order to use them in the case of large angle motion of the magnetization and/or in the presence of anisotropies.
- Investigation of edge modes in MTJ-elements of different sizes and shapes may lead to a better understanding of these modes and determination of their spatial confinement.
- A finite element method will be of extreme importance to perform numerical simulations on the *local* magnetization dynamics in the element.
- Switching experiments may be possible in elements with a uniaxial anisotropy in the direction perpendicular to the magnetic field pulse. However, in order to stroboscopically measure full switching, magnetic field pulses have to be applied that switch the magnetization back and forth.

Acknowledgements

In these last lines of this report I would like to thank all the people that made my last year as a student a very special one. First of all I thank Csaba Józsa, for his enthusiastic guidance the entire year, for always being available if I had questions or needed advice, and especially for helping me in writing this Thesis by giving corrections and useful suggestions in a very busy and sometimes hectic time for both of us. Secondly, I thank Bert Koopmans for creating the project I worked on, for his inspiring comments and suggestions, for having almost always the answers to my questions and for not holding me back from going to Hawai'i for a month, just when the laser labs where being renovated. I thank Henk Swagten for useful discussions about this work, Hans Boeve for making the MTJ-samples at Philips Research, Oleg Kurnosikov for his help in making the electrical contacts and Jef Noijen for fixing all kinds of electronics problems. Furthermore, I thank all the people of FNA for creating a nice scientific and social environment and for having a lot of fun at the parties in the coffee room.

I want to express many thanks to the members of "Evolutie" for having a great time in the 'Salon', in the Ardennen, in the French Alpes and in Hawai'i and for all the wonderful moments we've spent together, not only last year, but during my entire student life in Eindhoven. I thank the "Stiefelcommissie Natuurkunde", for the many relaxed evenings full of small talk, crap, laughter and of course a few "Stiefels" with beer. I also thank all the students at SVTN "J.D. van der Waals" with whom I've had lots of fun during all kinds of activities.

Finally, I thank my parents, for always being supportive during my period as a student in Eindhoven, even though it turned out to be somewhat more than five years. And last but not least, I thank Willy Mackus, for her support and for giving me, especially last year, the prospect of a wonderful future with the two of us.

Bibliography

[1] M.N. Baibich, J.M. Broto, A. Fert, F. Nguyen Van Dau, F. Petroff, P. Eitenne, G. Creuzet, A. Friederich and J. Chazelas, *Giant Magnetoresistance of (001)Fe/(001)Cr magnetic superlattices*, Phys. Rev. Let. **61**, 2472 (1988)

[2] H. Fukuzawa, K. Koi, H. Tomita, H.N. Fuke, Y. Kamiguchi, H. Iwasaki and M. Sahashi, *NOL specular spin-valve heads using an ultrathin CoFe free layer*, J. Magn. Magn. Mat. **235**, 208-212 (2001)

[3] J.S. Moodera, L.R. Kinder, T.M. Wong and R. Meservey, *Large magnetoresistance at room temperature in ferromagnetic thin film tunnel junctions*, Phys. Rev. Let. **74**, 3276 (1995)

[4] D. Wang, C. Nordman, J. Daughton, Z. Qian and J. Fink, *70% TMR at room temperature for SDT sandwich junctions with CoFeB as free and pinned layers*, In *Abstracts of the 9th joint MMM/Intermag conference*, page 87, Anaheim, Ca, (2004)

[5] M. van Kampen, *Ultrafast spin dynamics in ferromagnetic metals*, PhD Thesis, Eindhoven University of Technology (2003)

[6] B.N. Engel, N.D. Rizzo, J. Janesky, J.M. Slaughter, R. Dave, M. DeHerrera and M. Durlam, *The science and technology of magnetoresistive tunneling memory*, IEEE Trans. Nano. **1**, 32-37 (2002)

[7] M. Durlam et al., *A 0.18 μm 4Mb toggling MRAM*, IEEE International Electron Devices Meeting, 34.6.1-3, (2003)

[8] L. Landau and E.M. Lifshitz, *On the theory of dispersion of magnetic permeability in ferromagnetic bodies*, Phys. Z. Union **8**, 153-169 (1935)

[9] J. Miltat e.a. in *Spin dynamics in confined magnetic structures*, edited by B. Hillebrands and K. Ounadjela, Springer-Verlag, Berlin, (2002)

[10] C. Kittel, *Introduction to solid state physics*, John Wiley & Sons, Inc., New York, (1996)

[11] Landolt-Börnstein, *Numerical Data and Functional Relationships in Science and Technology - New Series III / 19A*, Springer Verlag, Heidelberg, (1986)

[12] C. Jozsa, J.H.H. Rietjens, M. van Kampen, E. Smalbrugge, M.K. Smit, W.J.M. de Jonge and B. Koopmans, *Retrieving pulse profiles from pump-probe measurements on magnetization dynamics*, J. Appl. Phys., accepted

[13] J.P. Park, P. Eames, D.M. Engebretson, J. Berezovksy and P.A. Crowell, *Spatially resolved dynamics of localized spin-wave modes in ferromagnetic wires*, Phys. Rev. Lett. **89**, 277201 (2002)

[14] Th. Gerrits, H.A.M. van den Berg, J. Hohlfeld, L. Bär and Th. Rasing, *Ultrafast precessional magnetization reversal by picosecond magnetic field pulse shaping*, Nature (London) **418**, 509-511 (2002)

[15] H.W. Schumacher, C. Chappert, P. Crozat, R.C. Sousa, P.P. Freitas, J. Miltat, J. Fassbender and B. Hillebrands, *Phase coherent precessional magnetization reversal in microscopic spin valve element*, Phys. Rev. Lett. **90**, 017201 (2003)

[16] K. van Sweevelt, Switching behavior of magnetic tunnel junctions in MRAM, Master Thesis, Eindhoven University of Technology (2003)

[17] C.-Y. You and S.-C. Shin, *Generalized analytic formulae for magneto-optical Kerr effects*, J. Appl. Phys. **84**, 541-546 (1998)

[18] L. Lagae, *Ultra-fast tiny magnets for magneto-electronic applications*, PhD Thesis, IMEC (2003)

[19] N.W.E. McGee, *The magneto-optical Kerr effect: Theory Measurement and Application*, Master Thesis, Eindhoven University of Technology (1991)

[20] W.K. Hiebert, A. Stankiewicz and M.R. Freeman, *Direct observation of magnetic relaxation in small Permalloy disk by time-resolved scanning Kerr microscopy*, Phys. Rev. Lett. **79**, 1134 (1997)

[21] F.L. Pedrotti, S.J. and L.S. Pedrotti, *Introduction to optics*, Prentice Hall International, Inc., New Jersey, (1996)

[22] Y. Acremann, C.H. Back, M. Buess, O. Portmann, A. Vaterlaus, D. Pescia and H. Melchior, *Imaging precessional motion of the magnetization vector*, Science **290**, 492-495 (2000)

[23] T.J. Silva, P. Kabos and M.T. Pufall, *Detection of coherent and incoherent spin dynamics during the magnetic switching process using vector-resolved nonlinear magneto-optics*, Appl. Phys. Let. **81**, 2205-2207, (2002)

[24] W.K. Hiebert, L. Lagae and J. de Boeck, *Spatially inhomogeneous ultrafast precessional magnetization reversal*, Phys. Rev. B **68**, 020402, (2003)

[25] R. C. O'Handley, *Modern magnetic materials, principles and application*, John Wiley & Sons, Inc., New York, (2000)